TAMPERE UNIVERSITY OF TECHNOLOGY

PEKKA ASTOLA

MODELING SOUND PROPAGATION AND INTERFERENCE PHENOMENA IN SHALLOW WATER ENVIRONMENT

Master of Science Thesis

Examiners: Professor Ioan Tabus and
Professor Bogdan Dumitrescu
Subject approved by the Faculty of Computing and Electrical Engineering on March 6, 2013

PREFACE

This Master of Science thesis has been written for the Department of Signal Processing at the Tampere University of Technology.

I wish to thank my supervisors Prof. Ioan Tabus and Prof. Bogdan Dumitrescu for their valuable comments and guidance. I would also like to extend my gratitude to my parents Jaakko and Ulla Astola for their encouragement and support during my studies.

Tampere, March 13, 2013

Pekka Astola
pekka.astola@tut.fi

TIIVISTELMÄ

TAMPEREEN TEKNILLINEN YLIOPISTO
Signaalinkäsittelyn ja tietoliikennetekniikan koulutusohjelma
PEKKA ASTOLA: MODELING SOUND PROPAGATION AND INTERFERENCE PHENOMENA IN SHALLOW WATER ENVIRONMENT
Diplomityö, 72 sivua, 3 liitesivua
Huhtikuu 2013
Pääaine: Signaalinkäsittely
Tarkastajat: Prof. Ioan Tabus ja Prof. Bogdan Dumitrescu
Avainsanat: vedenalainen ääni, interferenssi, monipolkuympäristö, äänen eteneminen

Ääni, joka saa alkunsa pinnalla tai veden alla kulkevassa aluksessa, heijastuu yleensä useita kertoja sekä pinnan että merenpohjan kautta ennen saapumistaan sensorille. Näiden useiden viivästettyjen äänisignaalien summautuminen synnyttää interferenssikuvion joka on erityinen jokaiselle erilaiselle monipolkuympäristölle. Passiivisessa vedenalaisessa tarkkailussa monipolkuisen äänen synnyttämä interferenssikuvio voidaan havaita aika-taajuus analyysilla kuten spektrogrammilla. Jos monipolkuympäristöä voidaan arvioida ja mallintaa, interferenssikuvio voidaan yhdistää lähteen parametreihin, kuten syvyyteen ja nopeuteen. Vedenalaisen äänen mallintaminen monipolkuympäristössä alkaa äänen fysikaalisella mallinnuksella aaltoyhtälöiden muodossa. Näitä differentiaaliyhtälöitä voidaan käyttää lähtökohtana paremmin lähestyttävien teoreettisten mallien muodostamisessa. Näistä malleista tunnetuimmat ovat sädeteoria sekä normaalimooditeoria. Yksi kaikkein oleellisimmista seikoista vedenalaisen äänen monipolkumallinuksessa on refraktio eli äänen taipuminen. Merivedessä tätä taipumista aiheuttaa ensisijaisesti meriveden vaihtuva lämpötila syvyyden suhteen. Säde- ja normaalimooditeoria kykenevät molemmat ottamaan refraktion huomioon.

Tässä opinnäytetyössä säde- ja normaalimooditeorian numeerisia malleja käytetään arvioimaan vedenalaisen aluksen aiheuttamaa interferenssikuviota. Työ sisältää numeerisen sädemallin kehittämisen, jota arvioidaan yhdessä kolmannen osapuolen säde- ja normaalimoodimallien kanssa. Tämä arviointi on tehty käyttäen oikeaa hydrografista dataa, jonka pohjalta todenmukaisia äänennopeusprofiileja on laskettu. Profiilit on valittu simuloimaan kolmea sijaintia Suomen rannikolla. Lopuksi työssä arvioidaan Lloydin peili-ilmiön käyttöä vedenalaisten alusten erottamisessa pinta-aluksista käyttäen pinta-aluksen synnyttämää heijastusta merenpohjasta.

ABSTRACT

TAMPERE UNIVERSITY OF TECHNOLOGY
Master's Degree Programme in Signal Processing and Communications Engineering
PEKKA ASTOLA: MODELING SOUND PROPAGATION AND INTERFERENCE PHENOMENA IN SHALLOW WATER ENVIRONMENT
Master of Science Thesis, 72 pages, 3 Appendix pages
April 2013
Major: Signal Processing
Examiners: Prof. Ioan Tabus and Prof. Bogdan Dumitrescu
Keywords: underwater sound, interference, multipath environment, sound propagation

Multipath propagation of underwater sound gives rise to both constructive and destructive interference. The sound which originates from a surface or a submerged source is reflected multiple times by the surface and the seabed before reaching the sensor. The summation of the many delayed replicas of the original signal results in an interference pattern specific to the current multipath environment. In passive underwater surveillance the multipath interference pattern can be detected using time-frequency analysis such as spectrograms. If the multipath environment can be approximated to some extent the patterns found in the spectrogram can be linked to certain source parameters, such as depth and speed. The theoretical modeling of underwater sound propagation in a multipath environment starts with the physical modeling of sound in the form of differential equations. These differential equations can be studied to give more approachable theories for sound propagation, most notably ray and normal mode theories. One of the most important aspects in modeling the multipath environment is refraction, or bending of sound imposed by the unavoidable temperature gradient found in all large bodies of water. Ray and normal mode theories are both capable of modeling the propagation of sound in vertical temperature gradients.

In this thesis numerical models of ray and normal mode theories are used to estimate the interference patterns created by a submerged vessel. This thesis includes the developement of a numerical ray model which is evaluated in together with third party ray and normal mode models. The evaluation is done using real hydrographic data to give realistic sound speed profiles at three locations on the Finnish coast. Further, the seabed reflection is assessed in the context of using Lloyd's mirror effect for passive detection.

LIST OF SYMBOLS AND ABBREVIATIONS

A	amplitude
a	acceleration
c	speed of sound
F	force
f_s	sampling frequency
$H_0^{(1)}$	Hankel function of the first kind
k_m	horizontal propagation constant
κ	bulk modulus
m	mass
n	index of refraction
ω	frequency
P	pressure
ϕ	phase
R	reflection coefficient
r	radius
ρ	density
S	salinity
σ	fractional density
T	temperature
t	time
θ	ray angle
u	particle velocity
v	volume
W	wavefront

$x(t)$	signal
$X(\omega)$	spectrum
z	acoustic impedance
DFT	discrete Fourier transform
FFT	fast Fourier transform
ppt	parts per thousand
SSP	sound speed profile
STFT	short-time Fourier transform

CONTENTS

1. Introduction 1
2. Physics of Underwater Sound 3
2.1 Derivation of the Wave Equation 3
2.2 Plane and Spherical Wave Solutions 7
2.3 Wavefront Propagation 11
2.4 Refraction 12
3. Speed of Sound in Seawater 15
3.1 Empirical Formulas 15
4. Sound Propagation in Seawater 21
4.1 Ray Theory 21
4.1.1 Generalization of a Ray 22
4.1.2 Eikonal Equation 23
4.1.3 Rays in Vertical Velocity Gradients 24
4.2 Normal Mode Theory 27
5. Multipath Propagation 28
5.1 Phase Change at the Boundaries 28
5.2 Ideal Model for Multipath Delays 29
5.3 Refraction and Multipath Delays 30
6. Computing Interference Patterns 32
6.1 Analog to Digital Conversion 32
6.2 Discrete Fourier Transform 33
6.3 Fast Fourier Transform 34
6.4 Time-frequency Analysis 34
6.4.1 Short-Time Fourier Transform 35
6.4.2 Interference Patterns on Spectrogram 35
6.4.3 Lloyd's Mirror Effect 36
7. Numerical Computation of the Acoustic Field 39
7.1 Matlab 39
7.1.1 The Ray Trace Algorithm 40
7.2 The Acoustics Toolbox 51
7.2.1 Structure 51
7.2.2 Environmental File 51
7.2.3 Field Parameter File 53
7.2.4 Running the Programs 53
8. Results and Discussion 54
8.1 Selection of Simulation Parameters 54
8.2 Monthly Variation in the Interference Images 56

8.3 Evaluating the Significance of Seabed Reflections 65
9. Conclusions 70
A. Appendix 73

LIST OF FIGURES

2.1 Plane wave p_i encountering a boundary at $x, y = 0$. 14

3.1 Sound speeds in the temperature of 17 °C and salinity range of 2-28 ppt (Baltic Sea). 19
3.2 Sound speeds in the salinity of 35 ppt (oceans) and temperature range of 2-22 °C. 19
3.3 Sound speeds in the salinity of 8 ppt (Baltic Sea) and temperature range of 2-22 °C. 20

4.1 A demonstration of the Huygens' principle for constructing successive wavefronts. The initial wavefront expands by a length of *cdt* in the direction of the normal. 22

6.1 Interference pattern for Lloyd's mirror phenomenon for a passing submarine example. 38
6.2 Spectrogram for Lloyd's mirror phenomenon for a passing submarine example. 38

7.1 Ray behaviour in case I. 44
7.2 Ray behaviour in case II. 46
7.3 Ray behaviour in case III 47
7.4 Ray behaviour in case IV. 49
7.5 The structure of the Acoustics Toolbox. Circles represent input and output files, rectangles executables. 51

8.1 Geometry of the simulation. Cross-sectional view on the left, plane view on the right. 55
8.2 Map of the simulated locations. Harmaja 1, Santio 2 and Utö 3. . . . 55
8.3 Sound speed profiles starting from left Harmaja, Santio and Utö. . . . 56
8.4 The interference image computed with rayTrace and Harmaja SSP using parameters from Table 8.1. Left in January, right in September. Water depth 30m. 58
8.5 The interference image computed with rayTrace and Santio SSP using parameters from Table 8.1. Left in January, right in September. Water depth 40m. 58
8.6 The interference image computed with rayTrace and Utö SSP using parameters from Table 8.1. Left in January, right in September. Water depth 80m. 58

8.7 The interference image computed with the ideal model and Harmaja SSP using parameters from Table 8.1. Left in January, right in September. Water depth 30m. 59
8.8 The interference image computed with the ideal model and Santio SSP using parameters from Table 8.1. Left in January, right in September. Water depth 40m. 59
8.9 The interference image computed with the ideal model and Utö SSP using parameters from Table 8.1. Left in January, right in September. Water depth 80m. 59
8.10 The interference image computed with BELLHOP and Harmaja SSP using parameters from Table 8.1. Left in January, right in September. Water depth 30m. 60
8.11 The interference image computed with BELLHOP and Santio SSP using parameters from Table 8.1. Left in January, right in September. Water depth 40m. 60
8.12 The interference image computed with BELLHOP and Utö SSP using parameters from Table 8.1. Left in January, right in September. Water depth 80m. 60
8.13 The interference image computed with the KRAKEN and Harmaja SSP using parameters from Table 8.1. Left in January, right in September. Water depth 30m. 61
8.14 The interference image computed with KRAKEN and Santio SSP using parameters from Table 8.1. Left in January, right in September. Water depth 40m. 61
8.15 The interference image computed with KRAKEN and Utö SSP using parameters from Table 8.1. Left in January, right in September. Water depth 80m. 61
8.16 Monthly variation in the transmission loss computed with rayTrace between January and September in Harmaja using parameters from Table 8.1. Water depth 30m. 62
8.17 Monthly variation in the transmission loss computed with rayTrace between January and September in Santio using parameters from Table 8.1. Water depth 40m. 62
8.18 Monthly variation in the transmission loss computed with rayTrace between January and September in Utö using parameters from Table 8.1. Water depth 80m. 62
8.19 Monthly variation in the transmission loss computed with the ideal model between January and September in Harmaja using parameters from Table 8.1. Water depth 30m. 62

8.20 Monthly variation in the transmission loss computed with the ideal model between January and September in Santio using parameters from Table 8.1. Water depth 40m. 63
8.21 Monthly variation in the transmission loss computed with the ideal model between January and September in Utö using parameters from Table 8.1. Water depth 80m. 63
8.22 Monthly variation in the transmission loss computed with BELLHOP between January and September in Harmaja using parameters from Table 8.1. Water depth 30m. 63
8.23 Monthly variation in the transmission loss computed with BELLHOP between January and September in Santio using parameters from Table 8.1. Water depth 40m. 63
8.24 Monthly variation in the transmission loss computed with BELLHOP between January and September in Utö using parameters from Table 8.1. Water depth 80m. 64
8.25 Monthly variation in the transmission loss computed with KRAKEN between January and September in Harmaja using parameters from Table 8.1. Water depth 30m. 64
8.26 Monthly variation in the transmission loss computed with the normal KRAKEN between January and September in Santio using parameters from Table 8.1. Water depth 40m. 64
8.27 Monthly variation in the transmission loss computed with KRAKEN between January and September in Utö using parameters from Table 8.1. Water depth 80m. 64
8.28 rayTrace with Utö SSP and the number of reflections per each path limited to 3 using parameters from Table 8.1. Water depth 80m. . . . 65
8.29 Interference image for the seabed reflection with a SNR of 42 dB. Bottom attenuation coefficient from the top 0, 1.5 and 3 dB. 67
8.30 Interference image for the seabed reflection with a SNR of 54 dB. Bottom attenuation coefficient from the top 4.5, 6 and 7.5 dB. 68
8.31 Interference image for the seabed reflection with a SNR of 60 dB. Bottom attenuation coefficient from the top 6, 7.5 and 9 dB. 69

LIST OF TABLES

3.1 Table of coefficients 18

5.1 Multipath delays in ideal model. 30
5.2 A realistic sound speed profile with depth, temperature, and salinity. 31
5.3 Multipath delays in the refracted model. 31
5.4 Difference in multipath delays between the refracted and the ideal model. 31

7.1 Variables used in rayTrace. 41
7.2 Sound velocity matrix $\boldsymbol{M}$. 41
7.3 Indexing the sound velocity matrix $\boldsymbol{M}$. 42
7.4 Values of θ_1 and g in case I. 43
7.5 Expressions for g and r in case I. 44
7.6 Rest of the variables for case I when ray bends back. 44
7.7 Rest of the variables for case I when next layer is bottom. 45
7.8 Rest of the variables for case I when ray continues to the next layer. . 45
7.9 Values of θ_1 and g in case II. 45
7.10 Rest of the variables for case II when next layer is bottom. 46
7.11 Rest of the variables for case II when ray continues to the next layer. 47
7.12 Values of θ_1 and g in case III. 47
7.13 Rest of the variables for case III when next layer is surface. 48
7.14 Rest of the variables for case III when ray continues to the next layer. 48
7.15 Values of θ_1 and g in case IV. 49
7.16 Expressions for g and r in case IV. 49
7.17 Rest of the variables for case IV when ray bends back. 50
7.18 Rest of the variables for case IV when next layer is surface. 50
7.19 Rest of the variables for case IV when ray continues to the next layer. 50

8.1 Simulation parameters. 55
8.2 Simulation parameters for the surface ship. 66

1. INTRODUCTION

Underwater acoustics encompasses of all types of problems in which sound propagates through water. The most notable field of study is of course the sonar followed by other means of underwater surveillance. This is due to the fact that underwater regions have and will remain beyond the scope of most civilian commerce. Excluding fishing, wreck diving and marine biology the most intensive study in underwater acoustics can be found in naval areas.

Eventhough the historical references to submerged sound can be found dating back to the 1490s the more intense scientific study has been around no more than 200 years. While the systematic study of seawater properties such as the temperature of the Baltic sea have been conducted since the 1770s [9] the first true study of underwater sound was perhaps the one by Colladon and Strum in 1827. The nineteenth century also saw the discovery of piezoelectricity and the invention of the carbon-button microphone also known as the earliest hydrophone. In 1912 the first airborne and underwater echo ranging devices were invented and by 1914 echo ranging was succesfully used to detect an iceberg two miles away [18]. The outbreak of World War I and the need for underwater surveillance further increased military interest in underwater sound. In 1919 the first scientific paper in underwater sound was published in Germany and described the theoretical bending of sound in temperature and salinity gradients. Being clearly ahead of its time the paper unfortunately remained unnoticed for almost 60 years [18]. After World War I the study of underwater sound went into slight hibernation but again erupted just before World War II.

A more modern developement in underwater surveillance is the use of digital computers and signal processing to both enhance and further analyze a recorded audio signal. Spectral methods study the ingredients of the recordings to for example classify sound sources, while the study of direction of arrival methods tries to determine the direction of the sound sources. In addition to analyzing recorded signals there is also the need for the theoretical modeling of how sound propagates in water. The propagation paths taken by underwater sound can become quite complex and its effects in the recorded signals quite substantial. The propagation of sound through multiple paths is known as multipath propagation and this phenomenon gives rise to specific transmission loss patterns in the recorded signal. These patterns can be

used to determine properties of the source only if the propagation paths themselves can be modeled accurately.

This thesis concentrates in modeling the sound propagation in shallow water. We start by giving the mathematical background of underwater sound in Chapter 2, followed by equations to compute the speed of sound in Chapter 3. The mathematical study is turned into theoretical models of sound propagation in Chapter 4, followed by the introduction of multipath propagation in Chapter 5. The mathematical and theoretical part of this thesis is finished by the introduction of the necessary signal processing in Chapter 6. This chapter also includes a short dicussion of the Lloyd's mirror effect.

Most of the hard work in this thesis went into Chapters 7 and 8. Specifically, a ray tracer based on the ray theory was developed on Matlab and used in together with third-party numerical models to compute transmission loss patterns. Chapter 7 contains the developement of the ray tracer in addition to the introduction of the third-party models. In Chapter 8 the models are evaluated in simulated scenarios which include a realistic source-hydrophone geometry under real sound speed profiles. Chapter 9 concludes this work with a summary of conclusions.

2. PHYSICS OF UNDERWATER SOUND

The accurate modeling of sound waves in any medium requires a mathematical method for combining the physical attributes, such as displacement of particles and the following pressure anomalies with time and space. In this section a second-order linear partial differential equation, known as the wave equation is derived to suit this purpose. This derivation is then followed by the presentation of two simple solutions and the discussion of wavefronts. In the last section of this chapter we introduce an important property of wavefront behaviour at the boundary of two media.

We include the derivation of the wave equation for underwater sound for two reasons. First, the wave equation is essential to this study as most of the results governing the propagation of sound follow from it and secondly, the elementary derivation of the equation presented here provides intuitive understanding of the physical phenomena that are behind sound propagation in water.

2.1 Derivation of the Wave Equation

The wave equation, or the differential equation for wave propagation, can be derived from four basic equations. These equations are the equation of continuity, the equations of motion, pressure related force equations, and the equation of state which relates the pressure changes to density changes. The derivation of the wave equation in this chapter is a more summarized version of the one presented in [8].

The first of the four basic equations, the equation of continuity states that no disturbance of a fluid can cause mass to be either created or destroyed. This leads to the conclusion that any difference between the amounts of fluid entering or leaving a volume must result in a corresponding change of density. For a fluid of density ρ passing at velocity $u = [u_x \; u_y \; u_z]$ through an infinitesimal cube of dimensions l_x, l_y and l_z the change in average density can be written as

$$\frac{\partial}{\partial t}[\rho l_x l_y l_z] = -\left[\frac{\partial(\rho u_x)}{\partial x} + \frac{\partial(\rho u_y)}{\partial y} + \frac{\partial(\rho u_x)}{\partial z}\right] l_x l_y l_z.$$

Canceling out the constant dimensions l_x, l_y, l_z we obtain the general equation of continuity

$$\frac{\partial \rho}{\partial t} = -\left[\frac{\partial(\rho u_x)}{\partial x} + \frac{\partial(\rho u_y)}{\partial y} + \frac{\partial(\rho u_x)}{\partial z}\right].$$

If we assume that the actual density ρ will not differ very much from the equilibrium density of ρ_0 we can define σ as

$$\sigma = \frac{\rho - \rho_0}{\rho_0}$$

where the newly defined σ is known as the fractional density or condensation. The introduction of σ leads to the simplified equation of continuity

$$\frac{\partial \sigma}{\partial t} = -\left(\frac{\partial u_x}{\partial x} + \frac{\partial u_y}{\partial y} + \frac{\partial u_z}{\partial z}\right). \tag{2.1}$$

The second basic equation used in deriving the wave equation is Newton's second law of motion. This law states that the product of a particle's mass and its acceleration in any direction equals the force acting on it in that direction. It can be written as

$$F = ma. \tag{2.2}$$

The velocity distribution within the fluid as a function of position and time is

$$u_x = u_x(x, y, z, t),\ etc.,$$

and the distribution of acceleration is

$$a_x = a_x(x, y, z, t),\ etc.$$

Since an acceleration is the first derivative of a velocity we can rewrite a_x, a_y, a_z as partial derivatives

$$a_x = \frac{\partial u_x}{\partial t};\quad a_y = \frac{\partial u_y}{\partial t};\quad a_z = \frac{\partial u_x}{\partial t}.$$

The mass of the fluid within the volume element v_0 is ρv_0. Using (2.2) we can write the components forces F_x, F_y, F_z as

$$F_x = \rho v_0 \frac{\partial u_x}{\partial t};\ F_y = \rho v_0 \frac{\partial u_y}{\partial t};\ F_z = \rho v_0 \frac{\partial u_z}{\partial t}.$$

We can rewrite the previous equations to be independent of the particular value of the small volume v_0 as

$$f_x = \rho \frac{\partial u_x}{\partial t};\quad f_y = \rho \frac{\partial u_y}{\partial t};\quad f_z = \rho \frac{\partial u_z}{\partial t} \tag{2.3}$$

where

$$f_x = \frac{F_x}{v_0};\ f_y = \frac{F_y}{v_0};\ f_z = \frac{F_z}{v_0}.$$

To derive the relationship with force and pressure in a fluid we must for practical

reasons rely on the assumption of a perfect fluid. Perfect fluids are incompressible and do not exhibit shear stress. When considering pressure in a fluid we disregard the effect of hydrostatic pressure, which is the vertical pressure caused by gravitional effects. Again, let us consider a cube of dimensions l_x, l_y, l_z and the forces acting in the x direction. If the pressure on one side is p, the total force on that surface is pl_xl_y. The pressure on the opposite side is clearly $p + (\partial p/\partial x)l_x$ and the total force on that surface is therefore $[p + (\partial p/\partial x)]l_xl_yl_z$. These two forces are parallel and the resultant can be obtained by subtraction. This leads to the total force on the volume v_0 in the x direction to be

$$F_x \equiv f_x v_0 = -\frac{\partial p}{\partial x} l_x l_y l_z.$$

Thus, the forces per unit volume are given by

$$f_x = -\frac{\partial p}{\partial x} \tag{2.4}$$

$$f_y = -\frac{\partial p}{\partial y} \tag{2.5}$$

$$f_z = -\frac{\partial p}{\partial z}. \tag{2.6}$$

For effective use the wave equation should only contain one dependent variable. So far the basic equations derived contain dependent variables σ, p, ρ, u_x, u_y, u_z. The variables σ and ρ are equivalent and the velocity components can be later eliminated using the equation of continuity. However, the relationship between density ρ and pressure p has to be established before we obtain a differential equation for the propagation of sound. This relationship is obtained from the equation of state.

Equation of state for any fluid describes the pressure as a function of density ρ and temperature T as

$$P = P(\rho, T).$$

This function has to be determined experimentally and varies with different fluids. We now make two assumptions. First, we assume that the deviations caused by the sound wave are only slightly different from the state of equilibrium and that the change in pressure is proportional to the fractional change in density. Second, it is assumed that the changes caused by the passing of the sound wave take place so rapidly that there is no conduction of heat. This leads to the assumption that the fractional change in density and the change in pressure are proportional to each other:

$$p = \kappa\sigma, \tag{2.7}$$

where p denotes the change in pressure, or excess pressure, and κ is a fluid specific

variable know as the bulk modulus and determines how much a given material will compress under a specific amount of pressure [22]. The bulk modulus for any fluid varies with its chemical structure, temperature, and pressure but for now it is treated as a constant.

We are now ready to use equation of continuity (2.1), the equations of motion (2.3), the law of forces (2.4), and the equation of state (2.7) to derive the wave equation for sound propagation in a fluid. From equation (2.7) we have

$$\frac{\partial p}{\partial x} = \kappa \frac{\partial \sigma}{\partial x}; \quad \frac{\partial p}{\partial y} = \kappa \frac{\partial \sigma}{\partial y}; \quad \frac{\partial p}{\partial z} = \kappa \frac{\partial \sigma}{\partial z}. \tag{2.8}$$

By substituting these values for $\partial\sigma/\partial x$, $\partial\sigma/\partial y$, and $\partial\sigma/\partial z$ in the law of forces (2.4) we obtain

$$f_x = -\kappa \frac{\partial \sigma}{\partial x}; \quad f_y = -\kappa \frac{\partial \sigma}{\partial y}; \quad f_z = -\kappa \frac{\partial \sigma}{\partial z}. \tag{2.9}$$

After these values are substituted into the equations of motion (2.3), we obtain the following relations:

$$\rho \frac{\partial u_x}{\partial t} = -\kappa \frac{\partial \sigma}{\partial x} \tag{2.10}$$

$$\rho \frac{\partial u_y}{\partial t} = -\kappa \frac{\partial \sigma}{\partial y} \tag{2.11}$$

$$\rho \frac{\partial u_z}{\partial t} = -\kappa \frac{\partial \sigma}{\partial z}. \tag{2.12}$$

Since we assume that the density and velocity changes are comparatively small, the expressions $\rho\partial u_x/\partial t$ and $\rho_0\partial u_x/\partial t$ can be regarded equal. Then equations (2.10, 2.11 and 2.12) become

$$\rho_0 \frac{\partial u_x}{\partial t} + \kappa \frac{\partial \sigma}{\partial x} = 0 \tag{2.13}$$

$$\rho_0 \frac{\partial u_y}{\partial t} + \kappa \frac{\partial \sigma}{\partial y} = 0 \tag{2.14}$$

$$\rho_0 \frac{\partial u_z}{\partial t} + \kappa \frac{\partial \sigma}{\partial z} = 0. \tag{2.15}$$

In order to apply the equation of continuity (2.1) we differentiate equation (2.13) with respect to x, equation (2.14) with respect to y, and equation (2.15) with respect to z. The equations are added, leading to

$$\rho_0 \frac{\partial}{\partial t} \left(\frac{\partial u_x}{\partial x} + \frac{\partial u_y}{\partial y} + \frac{\partial u_z}{\partial z} \right) + \kappa \left(\frac{\partial^2 \sigma}{\partial x^2} + \frac{\partial^2 \sigma}{\partial y^2} + \frac{\partial^2 \sigma}{\partial z^2} \right) = 0. \tag{2.16}$$

The first parenthesis is $-\partial\sigma/\partial t$ from the equation of continuity (2.1) and equation

(2.16) reduces to

$$\frac{\partial^2\sigma}{\partial t^2} = \frac{\kappa}{\rho_0}\left(\frac{\partial^2\sigma}{\partial x^2} + \frac{\partial^2\sigma}{\partial y^2} + \frac{\partial^2\sigma}{\partial z^2}\right). \tag{2.17}$$

Since $\sigma = p/\kappa$ is from equation (2.7) equation (2.17) implies

$$\frac{\partial^2 p}{\partial t^2} = \frac{\kappa}{\rho_0}\left(\frac{\partial^2 p}{\partial x^2} + \frac{\partial^2 p}{\partial y^2} + \frac{\partial^2 p}{\partial z^2}\right).$$

It is convenient to set

$$c^2 = \frac{\kappa}{\rho_0}, \tag{2.18}$$

so that the wave equation becomes

$$\frac{\partial^2 p}{\partial t^2} = c^2\left(\frac{\partial^2 p}{\partial x^2} + \frac{\partial^2 p}{\partial y^2} + \frac{\partial^2 p}{\partial z^2}\right). \tag{2.19}$$

The wave equation (2.19) can now be used to give the time derivatives and the space derivatives of the pressure in a fluid through which the sound is passing. With acoustic methods, the sound intensity at any point and time can be computed from the pressure distribution given by the wave equation (2.19).

2.2 Plane and Spherical Wave Solutions

A more detailed description of the following solutions is given in [8].

For a plane wave traveling in the x direction the equation (2.19) reduces to

$$\frac{\partial^2 p}{\partial t^2} = c^2\frac{\partial^2 p}{\partial x^2}. \tag{2.20}$$

It is well known that the functions p which satisfy the equation (2.20) have the form of $f(t-x/c)$ and $f(t+x/c)$, where t is an arbitrary function, or a linear combination of two such functions. Let us focus on all the solutions of equation (2.20) which have the form

$$p = f(t - x/c).$$

Although there are infinite number of possible choices of f only one of them can fit a particular physical situation. Suppose that for some physical situation, or initial and boundary conditions, there is one member of the family of f, denoted by $f_1(t-x/c)$, which satisfies the initial and boundary conditions. Then a fixed value of $(t - x/c)$ will correspond to a specific value of excess pressure. For example, $p = f_1(4.13)$ would always be associated with a specific value of p. If this value is, say 0.02 then the excess pressure p will always have the value 0.02 when $(t - x/c) = 4.13$. That is, where

$$x = ct - 4.13c. \tag{2.21}$$

As the time t increases the excess pressure p travels in the positive x direction with the speed c since the value of equation (2.21) increases with t. Similarly, for a f of form $f_2(t + x/c)$ the excess pressure p will travel in the negative x direction with the speed c.

The initial conditions can be set for example in time t or space x. Two examples can be considered for a plane wave traveling in an infinite homogeneous medium or with no boundary conditions. In the first example the initial condition for the plane wave is set in space at a specific time t. Let us assume for time instant $t = 0$ and between the planes $x = 0$ and $x = x_0$, the exact excess pressure distribution is $p(x, 0) = \bar{p}(x)$. The excess pressure is zero at $t = 0$ for all values of x less than 0 or greater than x_0. If we assume that this initial disturbance gives rise to a traveling plane wave in the positive x direction, or that the solution is in the form of $p = f(t - x/c)$, then the solution of the wave equation with these conditions is

$$p(x, t) = \bar{p}(x - ct).$$

At the time t the intial disturbance will be duplicated between the planes $x = ct$ and $x = x_0 + ct$.

In the second example the initial condition of excess pressure is specified at a specific location of space x for the total time interval between $t = 0$ and $t = t_0$ by $p(0, t) = \bar{p}(t)$. The excess pressure at the plane $x = 0$ is zero for $t < 0$ and $t > t_0$. As in the first example we assume that this initial disturbance gives rise to a traveling plane wave in the positive x direction and the solution becomes

$$p(x, t) = \bar{p}(t - \frac{x}{c}). \tag{2.22}$$

If the intial disturbance $\bar{p}(x, y, z)$ or $\bar{p}(t)$ is not an arbitary function but a more specific harmonic vibration, such as a tone or a sonar pulse, then the initial disturbance is set by trigonometric functions. Suppose that the initial disturbance of the plane $x = 0$ in the second example is set by

$$\bar{p}(t) = a \cos(2\pi\omega t - \phi)$$

for values of t between 0 and t_0. Just as in equation (2.22) the solution has the form

$$p(x, t) = \bar{p}(t \pm \frac{x}{c}).$$

Thus, for plane waves traveling in a single direction the solution of the wave equation

with the intial conditions becomes

$$p = a\cos(2\pi\omega t + \frac{x}{c} - \phi)$$

or

$$p = a\cos(2\pi\omega t - \frac{x}{c} - \phi).$$

The amplitude of the pressure changes is at most a, ω is the frequency, and ϕ represents the phase.

If instead of plane waves we consider the source as a point source radiating acoustic energy in all directions instead of one, the function of excess pressure p has the form

$$p = p(r, t),$$

where r is the range. For spherical waves the range r is defined

$$r^2 = x^2 + y^2 + z^2,$$

from which it follows

$$\frac{\partial r}{\partial x} = \frac{x}{r}, \ \frac{\partial r}{\partial y} = \frac{y}{r}, \ \frac{\partial r}{\partial z} = \frac{z}{r}. \tag{2.23}$$

We use the relation (2.23) to calculate $\partial^2 p/\partial x^2$, $\partial^2 p/\partial y^2$, $\partial^2 p/\partial z^2$ in terms of r and the derivatives of p with respect to r. We can write

$$\frac{\partial p}{\partial x} = \frac{\partial p}{\partial r}\frac{\partial r}{\partial x} = \frac{\partial p}{\partial r}\frac{x}{r}$$

because spatially p depends only on r. By differentiating again,

$$\frac{\partial^2 p}{\partial x^2} = \frac{\partial p}{\partial r}\left[\frac{r^2 - x^2}{r^3}\right] + \frac{x^2}{r^2}\frac{\partial^2 p}{\partial r^2}.$$

Similarly, we can show that

$$\frac{\partial^2 p}{\partial y^2} = \frac{\partial p}{\partial r}\left[\frac{r^2 - y^2}{r^3}\right] + \frac{y^2}{r^2}\frac{\partial^2 p}{\partial r^2}$$

$$\frac{\partial^2 p}{\partial z^2} = \frac{\partial p}{\partial r}\left[\frac{r^2 - z^2}{r^3}\right] + \frac{z^2}{r^2}\frac{\partial^2 p}{\partial r^2}.$$

To obtain the right hand side of the wave equation (2.19) we add the previous expressions for $\partial^2/\partial x^2$, $\partial^2/\partial y^2$ and $\partial^2/\partial z^2$ and we get

$$\frac{\partial^2 p}{\partial x^2} + \frac{\partial^2 p}{\partial y^2} + \frac{\partial^2 p}{\partial z^2} = \frac{\partial^2 p}{\partial r^2} + \frac{2}{r}\frac{\partial p}{\partial r}.$$

The latter expression can be verified as $(1/r)(\partial^2/\partial r^2)(rp)$, so we obtain

$$\frac{\partial^2 p}{\partial x^2} + \frac{\partial^2 p}{\partial y^2} + \frac{\partial^2 p}{\partial z^2} = \frac{1}{r}\frac{\partial^2}{\partial r^2}(rp),$$

and the general wave equation (2.19) reduces to

$$\frac{\partial^2 (rp)}{\partial t^2} = c^2 \frac{\partial^2}{\partial r^2}(rp). \tag{2.24}$$

The equation (2.24) has a similar form to the equation (2.20) and is satisfied by

$$rp = f\left(t \pm \frac{r}{c}\right).$$

The general solution of equation (2.24) is in the form of

$$p(r,t) = \frac{f_1\left(t - \frac{r}{c}\right) + f_2\left(t + \frac{r}{c}\right)}{r}.$$

Consider the initial disturbance confined to a spherical shell of infinitesimal thickness at a distance of $r = r_0$. Assume that the excess pressure in this spherical shell source is given by

$$p(r_0,t) = \frac{\bar{p}(t)}{r_0}$$

between times $t = 0$ and $t = t_0$. Assume also that the excess pressure at points outside the shell is zero at time $t = 0$. For this initial condition the following solution is obtained

$$p(r,t) = c_1 \frac{\bar{p}\left(t - \frac{r}{c}\right)}{r} + (1 - c_1)\frac{\bar{p}\left(t + \frac{r}{c}\right)}{r}.$$

Physically, we can eliminate the solution $(1/r)\bar{p}(t+r/c)$ since it corresponds to wave which travels in the negative r direction or in other words is a wave which contracts into the origin at the time $t = 0$.

If the source is harmonic the initial conditions are of form

$$p = \frac{a\cos(2\pi\omega t - \phi)}{r_0},$$

and if r_0 is nearly zero the excess pressure p at distance r and time t is given by

$$p = \frac{a\cos(2\pi\omega(t - \frac{r}{c}) - \phi)}{r_0}.$$

2.3 Wavefront Propagation

For any propagating wave motion the postulate of wavefront describes all the points in space in which at any instant the points are in phase. For plane waves wavefronts are parallel planes traveling outward from the source. For spherical waves wavefronts are spherical surfaces traveling outward from the source with increasing radius.

For a mathematical study of wavefronts let us consider harmonic sound waves which are generated by a source undergoing a single-frequency vibration. To do this we must first derive the complex representation of harmonic vibrations. The following derivation follows the one given in [8].

The complex number $e^{i\omega}$ is defined by the equation

$$e^{iw} = \cos\omega + i\sin\omega,$$

where $i^2 = -1$. The one-dimensional harmonic vibration

$$d = a\cos\left(2\pi f(t-\epsilon)\right)$$

can be regarded as the real part of $ae^{i2\pi f(t-\epsilon)}$ or $Re\left(ae^{i2\pi f(t-\epsilon)}\right)$. This can be expressed as

$$D = ae^{i2\pi f(t-\epsilon)}, \tag{2.25}$$

where the actual physical displacement is $Re(D)$ and the numerical value for this displacement is the real part of the right-hand side of the equation or $Re\left(ae^{i2\pi f(t-\epsilon)}\right)$. Equation (2.25) can be written as

$$D = Ae^{i2\pi ft},$$

where A is the complex number $ae^{-i2\pi f\epsilon}$.

Let us now use the complex representation to find the harmonic solution of the plane wave equation (2.20). To begin we assume that

$$p(x,t) = Ae^{2\pi i(ft+mx)} \tag{2.26}$$

and see if there is a value of m to make equation (2.26) a solution of equation (2.20). By substituting equation (2.26) into equation (2.20) we get

$$(2\pi if)^2 p = c^2(2\pi im)^2 p.$$

From this we find that a value of m equal to f/c or $-f/c$ makes the equation (2.26)

a solution of the plane wave equation (2.20). The two solutions are,

$$p = Ae^{2\pi if[t\pm(x/c)]}; \quad A = ae^{-2\pi if\epsilon}. \tag{2.27}$$

Now we can move on to generalize the defintion of wave fronts for single-frequency harmonic vibrations. As seen from equation (2.27) the pressure at any point inside a fluid can be expressed as having the form

$$p = A(x, y, z)e^{i\theta(x,y,z,t)} \tag{2.28}$$

in which the phase angle θ at each point in space increases with time as

$$\theta = 2\pi f[t - \epsilon(x, y, z)]. \tag{2.29}$$

A wavefront is defined by all points at which the phase angle θ has a specified value. If the specified value is for example θ_0 then at any time t this wavefront, or surface, is defined by the equation

$$\epsilon(x, y, z) = t - \frac{\theta_0}{2\pi f}. \tag{2.30}$$

For later convenience when dealing with ray theory we replace $\epsilon(x, y, z)$ by an expression $W(x, y, z)/c_0$, in which c_0 is the speed of sound under certain conditions. Equation (2.30) now takes the form

$$p = A(x, y, z)e^{2\pi if[t-\frac{W(x,y,z)}{c_0}]}. \tag{2.31}$$

The defining equation of an individual wavefront now becomes

$$W(x, y, z) = c_0(t - t_0), \tag{2.32}$$

where

$$t_0 = \frac{\theta_0}{2\pi f}.$$

With different wavefronts the value of t_0 changes, but for a specific wavefront t_0 remains constant. It is also important to notice that W has the dimension of a length. This property becomes essential to the ray theory.

2.4 Refraction

When an acoustic wavefront strikes a boundary separating two media, the wave is both transmitted into the second medium and reflected back into the current medium. The physical phenomenon of a wave passing from one medium to another is known as refraction. Refraction and reflection change both the amplitude, direction

and phase of a wavefront and since ray theory relies on the concept of wavefronts it is necessary to be able to formulate the behaviour of a wavefront in the presence of a refractive boundary. In this section we derive the very useful Snell's law of refraction by studying the behaviour of a plane wave hitting a boundary between two media. This section is summarized from [8].

Consider a plane wave hitting a boundary at $y = 0$ as illustrated in Figure 2.1. We describe the plane wave by the equation (2.26) with x replaced by $x \sin\theta_i + y \cos\theta_i$, where θ_i denotes the incident angle of the wavefront. Now, for the incident wave we have

$$p_i = A_i e^{2\pi i f\left(t - \frac{x \sin\theta_i + y\cos\theta_i}{c}\right)}, \tag{2.33}$$

where p_i is the sound pressure of the incident wave and A_i its complex amplitude. Since the sound is both reflected and transmitted at the boundary we must consider two new variables,

$$p_r = A_r e^{2\pi i f\left(t - \frac{x \sin\theta_r - y\cos\theta_r}{c}\right)}, \tag{2.34}$$

$$p_t = A_t e^{2\pi i f\left(t - \frac{x \sin\theta_t + y\cos\theta_t}{c_1}\right)}, \tag{2.35}$$

where r stands for reflection and t for transmission or refraction. The sign of y is different between equations (2.34) and (2.35) since the two new wavefronts now travel in opposite y-directions.

The total pressure in the first medium is the sum of the incident and reflected waves. Denoting this total pressure by p we have,

$$p = p_i + p_r = A_i e^{2\pi i f\left(t - \frac{x \sin\theta_i + y\cos\theta_i}{c}\right)} + A_r e^{2\pi i f\left(t - \frac{x \sin\theta_r - y\cos\theta_r}{c}\right)}. \tag{2.36}$$

Now, the pressure must be the same on both sides of the boundary and therefore, $p_t + p_r = p_i$ at $y = 0$. This can be expressed as,

$$A_i e^{2\pi i f\left(t - \frac{x\sin\theta_i}{c}\right)} + A_r e^{2\pi i f\left(t - \frac{x\sin\theta_r}{c}\right)} = A_t e^{2\pi i f\left(t - \frac{x\sin\theta_t}{c_1}\right)},$$

or

$$e^{2\pi i f t}\left[A_i e^{-2\pi i f \frac{sin\theta_i x}{c}} + A_r e^{-2\pi i f \frac{sin\theta_r x}{c}} - A_t e^{-2\pi i f \frac{sin\theta_t x}{c_1}}\right] = 0 \tag{2.37}$$

for all values of t and x. The sum of the three harmonic functions of x in equation (2.37) can vanish only if their periods are the same. From this it follows that

$$\frac{\sin\theta_t}{c_1} = \frac{\sin\theta_i}{c} = \frac{\sin\theta_r}{c}, \tag{2.38}$$

and this implies that $\theta_i = \theta_r$, also known as the law of reflection [22]. This result is important and means that the angle of incident is the same as the angle of reflection.

Furthermore, the first equation of (2.38) can be rewritten as,

$$\frac{\sin\theta_i}{\sin\theta_t} = \frac{c}{c_1}, \tag{2.39}$$

a relation known as the law of refraction or Snell's law [22]. Equation (2.39) can now be used to estimate the direction of a wavefront when it passes between layers of media with different speeds of sound.

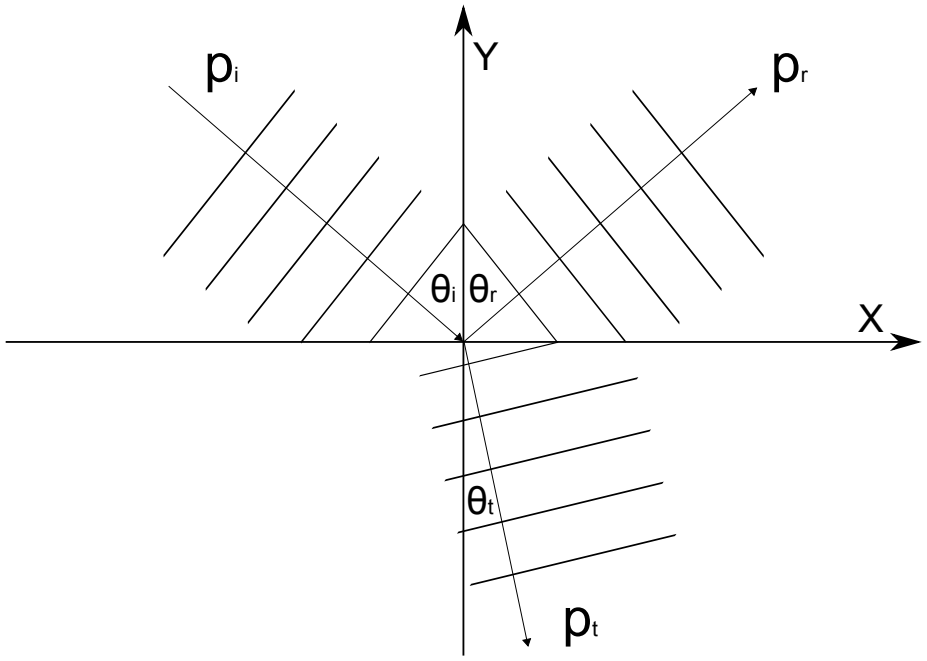

Figure 2.1: Plane wave p_i encountering a boundary at $x, y = 0$.

3. SPEED OF SOUND IN SEAWATER

Wave speed, speed of sound or sound velocity are all used to describe the speed at which a wave propagates in a medium. This property is known to especially depend on the temperature and chemical composition of the fluid or liquid. In the lack of actual measurements or with purely theoretical scenarios the speed of sound has to be somehow determined. In this chapter expressions for estimating the speed of sound are presented.

The history for measuring the speed of sound in water bodies dates back to 1827. The method was to measure the time of arrival difference for a submerged and an airborne sound source. The test was carried out in Lake Geneva and the result, 1435 m/s at 8.1 °C, is surprisingly close to modern measurements [18]. A more general approach taken by subsequent studies have not only measured the time of arrival but attempted to relate oceanographic parameters such as temperature, salinity, and depth to the speed of sound. These relationships can be established by either theoretic treatment or by direct measurements in well regulated conditions. Results from these studies have shown that the speed of sound increases with temperature, salinity, and depth. As both temperature and salinity vary with depth, time of day, and season the task of accurately modeling the speed of sound grows ever more complex. For example surface-ship echo ranging performs poorest during the afternoon and this phenomenon is referred as the "afternoon effect" [18]. Subtle or less subtle effects such as currents or geographical features like river mouths with heavy outputs of salinity decreasing fresh water further complicate the issue.

In this work the focus for the physical modeling of the medium is centered around the conditions found in the Baltic Sea. As a brackish sea the average salinity of the Baltic Sea is substantially lower than the oceanic averages, 7 parts per thousand (ppt) [9] compared to 35 ppt found in the oceans [7]. The history of the hydrographic study of the Baltic Sea dates back to 1770's when the first temperature measurements were made and regular hydrographic research began in Finland in 1898 [9].

3.1 Empirical Formulas

The sole use of equation (2.18) gives only a rough approximation for the velocity of sound in non-distilled water. Carefully conducted laboratory experiments have yield

expressions for the velocity of sound in terms of the three quantities: temperature, salinity, and pressure [18]. Simple formulas such as Del Grosso [4] and Wilson [20] have long been used and can be simplified for calculations by hand or a calculator. Algorithms such as the Chen and Millero [2], also known as the UNESCO algorithm [6], offer more complexity and accuracy. The coefficients of the Chen and Millero formula were revised by Wong and Shu [21] to accomodate the adoption of the International Temperature Scale of 1990 (ITS-90).

Del Grosso [4], 1952:

$$\begin{aligned} c = {} & 1448.6 + 4.618T - 0.0523T^2 + 1.25(S-35) \\ & - 0.011(S-35)(T) + 0.0027 \cdot 10^{-5}(S-35)T^4 \\ & - 2 \cdot 10^{-7}(S-35)^4(1 + 0.577T - 0.0072T^2) \end{aligned} \tag{3.1}$$

where T is temperature (°C) and S is salinity as ppt.

Wilson [20], 1960:

$$c = 1449.22 + \Delta V_T + \Delta V_P + \Delta V_S + \Delta V_{STP} \tag{3.2}$$

where,

$$\begin{aligned} \Delta V_T &= 4.6233T - 5.4585 \cdot 10^{-2}T^2 + 2.822 \cdot 10^{-4}T^3 - 5.07 \cdot 10^{-7}T^4 \\ \Delta V_P &= 1.60518 \cdot 10^{-1}P + 1.0279 \cdot 10^{-5}P^2 + 3.451 \cdot 10^{-9}P^3 - 3.503 \cdot 10^{-12}P^4 \\ \Delta V_S &= 1.391(S-35) - 7.8 \cdot 10^{-2}(S-35)^2 \\ \Delta V_{STP} &= (S-35)(-1.197 \cdot 10^{-2}T + 2.61 \cdot 10^{-4}P - 1.96 \cdot 10^{-7}P^2 \\ &\quad - 2.09 \cdot 10^{-6}PT) + P(-2.796 \cdot 10^{-4}T + 1.3302 \cdot 10^{-5}T^2 \\ &\quad - 6.644 \cdot 10^{-8}T^3) + P^2(-2.391 \cdot 10^{-7}T + 9.286 \cdot 10^{-10}T^2) - 1.745 \cdot 10^{-10}P^3T \end{aligned}$$

where P is pressure (kPa or kg/cm^2).

Chen and Millero [2; 6] (revised by Wong and Shu [21]), 1977:

$$c = C_W + AS + BS^{3/2} + DS^2 \tag{3.3}$$

where,

$$
\begin{aligned}
C_W &= (C_{00} + C_{01}T + C_{02}T^2 + C_{03}T^3 + C_{04}T^4 + C_{05}T^5) \\
&\quad + (C_{10} + C_{11}T + C_{12}T^2 + C_{13}T^3 + C_{14}T^4)P \\
&\quad + (C_{20} + C_{21}T + C_{22}T^2 + C_{23}T^3 + C_{24}T^4)P^2 \\
&\quad + (C_{30} + C_{31}T + C_{32}T^2)P^3 \\
A &= (A_{00} + A_{01}T + A_{02}T^2 + A_{03}T^3 + A_{04}T^4) \\
&\quad + (A_{10} + A_{11}T + A_{12}T^2 + A_{13}T^3 + A_{14}T^4)P \\
&\quad + (A_{20} + A_{21}T + A_{22}T^2 + A_{23}T^3)P^2 \\
&\quad + (A_{30} + A_{31}T + A_{32}T^2)P^3 \\
B &= B_{00} + B_{01}T + (B_{10} + B_{11}T)P \\
D &= D_{00} + D_{10}P,
\end{aligned}
$$

and where the coefficients can be found in Table 3.1.

As for all empirical formulas none of these expressions yield the exact same results since they are based on a specific sample and laboratory setup. Under definite circumstances some might be more suitable over the other. For example the parameters for Wilson's measurements for seawater ranged from $-3\,^{\circ}\mathrm{C}$ to $30\,^{\circ}\mathrm{C}$, 1.01 to 981 bars of pressure and 33 to 37 ppt for salinity [20]. Del Grosso measured at 1 atm pressure for seawater from $0\,^{\circ}\mathrm{C}$ to $40\,^{\circ}\mathrm{C}$ and 19 to 41 ppt for salinity [4]. Chen and Millero measured for seawater from $0\,^{\circ}\mathrm{C}$ to $40\,^{\circ}\mathrm{C}$, 0 to 1000 bars for pressure and 5 to 40 ppt for salinity [2]. Wilson [20] states that 99.5% of all seawater falls in the temperature range of $-3\,^{\circ}\mathrm{C}$ to $30\,^{\circ}\mathrm{C}$ and in the salinity range of 33 to 37 ppt. Brackish bodies of water such as the Baltic Sea falls in the 0.5% which is only partially covered by the previous salinity range. For the Baltic Sea salinity ranges from roughly 3 ppt in near shore areas to almost 30 ppt towards the Atlantic [5]. One must bear this in mind when choosing the appropriate formula to estimate sound velocity in a specific region.

Figure 3.1 demonstrates equations (3.1, 3.2, 3.3) in salinities covering the range which could be found in the Baltic Sea. The temperature and pressure are set to typical surface conditions during the summer ($17\,^{\circ}\mathrm{C}$ and 1 atm pressure). Figure 3.2 displays how well all three formulas agree when salinity is set to typical ocean levels. The formula derived by Wilson performs significantly differently in low salinity levels compared to Del Grosso or Chen and Millero as can be seen in Figure 3.1 and Figure 3.3.

Coefficients	Numerical values	Coefficients	Numerical values
C_{00}	1402.388	A_{02}	$7.166 \cdot 10^{-5}$
C_{01}	5.03830	A_{03}	$2.008 \cdot 10^{-6}$
C_{02}	$-5.81090 \cdot 10^{-2}$	A_{04}	$-3.21 \cdot 10^{-8}$
C_{03}	$3.3432 \cdot 10^{-4}$	A_{10}	$9.4742 \cdot 10^{-5}$
C_{04}	$-1.47797 \cdot 10^{-6}$	A_{11}	$-1.2583 \cdot 10^{-5}$
C_{05}	$3.1419 \cdot 10^{-9}$	A_{12}	$-6.4928 \cdot 10^{-8}$
C_{10}	0.153563	A_{13}	$1.0515 \cdot 10^{-8}$
C_{11}	$6.8999 \cdot 10^{-4}$	A_{14}	$-2.0142 \cdot 10^{-10}$
C_{12}	$-8.1829 \cdot 10^{-6}$	A_{20}	$-3.9064 \cdot 10^{-7}$
C_{13}	$1.3632 \cdot 10^{-7}$	A_{21}	$9.1061 \cdot 10^{-9}$
C_{14}	$-6.1260 \cdot 10^{-5}$	A_{22}	$-1.6009 \cdot 10^{-10}$
C_{20}	$3.1260 \cdot 10^{-5}$	A_{23}	$7.994 \cdot 10^{-12}$
C_{21}	$-1.7111 \cdot 10^{-6}$	A_{30}	$1.100 \cdot 10^{-10}$
C_{22}	$2.5986 \cdot 10^{-8}$	A_{31}	$6.651 \cdot 10^{-12}$
C_{23}	$-2.5353 \cdot 10^{-8}$	A_{32}	$-3.391 \cdot 10^{-13}$
C_{24}	$1.0415 \cdot 10^{-12}$	B_{00}	$-1.922 \cdot 10^{-2}$
C_{30}	$-9.7729 \cdot 10^{-9}$	B_{01}	$-4.42 \cdot 10^{-5}$
C_{31}	$3.8513 \cdot 10^{-10}$	B_{10}	$7.3637 \cdot 10^{-5}$
C_{32}	$-2.3654 \cdot 10^{-12}$	B_{11}	$1.7950 \cdot 10^{-7}$
A_{00}	1.389	D_{00}	$1.727 \cdot 10^{-3}$
A_{01}	$-1.262 \cdot 10^{-2}$	D_{10}	$-7.9836 \cdot 10^{-6}$

Table 3.1: Table of coefficients

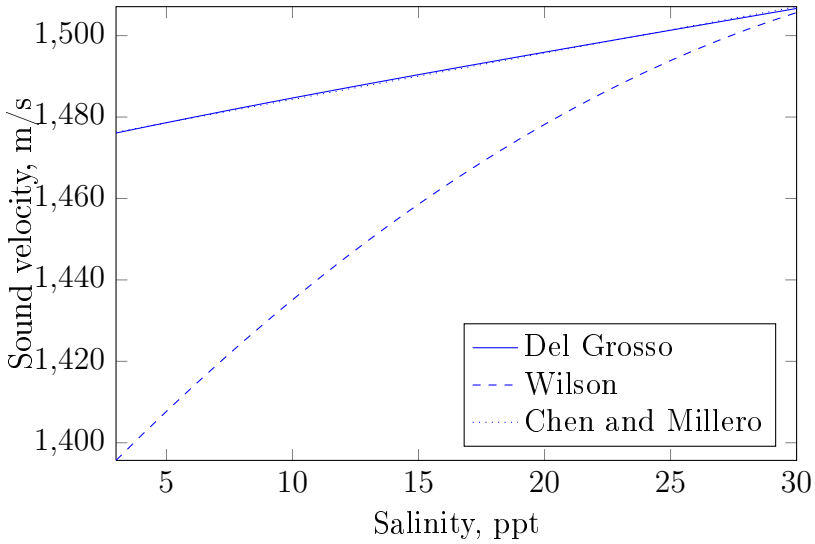

Figure 3.1: Sound speeds in the temperature of 17 °C and salinity range of 2-28 ppt (Baltic Sea).

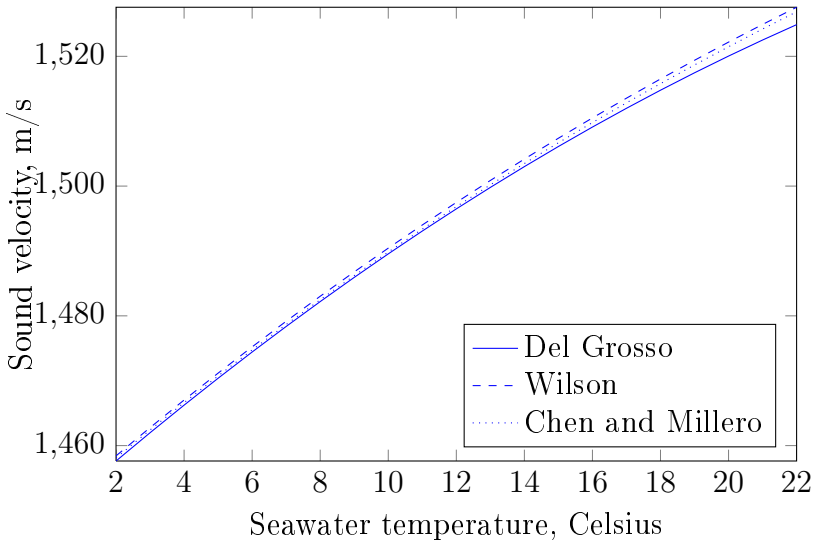

Figure 3.2: Sound speeds in the salinity of 35 ppt (oceans) and temperature range of 2-22 °C.

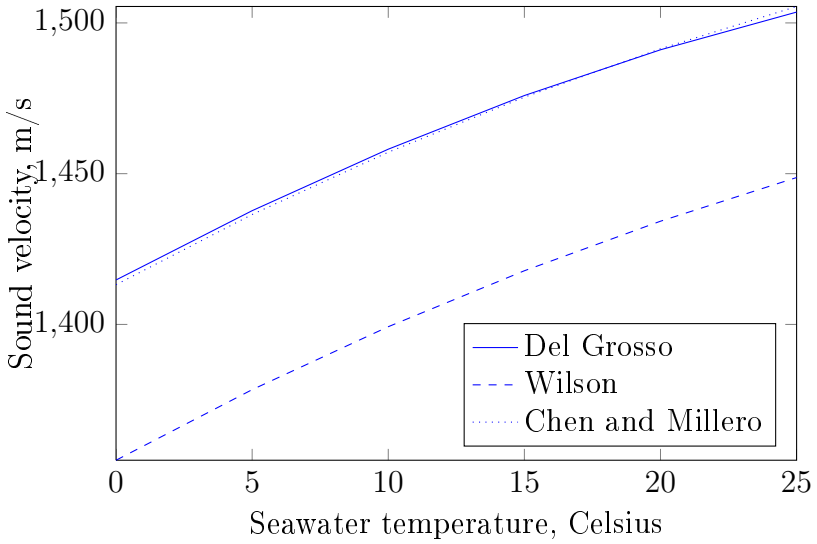

Figure 3.3: Sound speeds in the salinity of 8 ppt (Baltic Sea) and temperature range of 2-22 °C.

4. SOUND PROPAGATION IN SEAWATER

The mathematical treatment for sound propagation was given in Chapter 2 in the form of the wave equation. Unfortunately, the wave equation cannot be directly used to predict the behaviour of underwater sound. The postulated model includes too many simplifications such as seawater being a homogenic medium, the surface being a perfectly reflecting plane and the bottom having infinite density. Even this already heavily simplified view of the problem can be solved rigorously only for simple cases. More complex scenarios are not only difficult but often impossible to formulate. Even if the conditions can be exactly formulated they are still computationally expensive to solve. Nevertheless, the wave equation is the theoretical basis for all mathematical models of acoustic propagation.

There are essentially four types of models to describe sound propagation in the sea: spectral, normal mode, ray, and parabolic equation models [10]. These models are derived from the wave equation but employ assumptions and simplifications and should therefore be regarded as computationally reasonable approximations of the full solutions. Additionally, finite element or finite difference methods can be used to produce solutions of the full wave equation but their importance is rather limited due to their excessive computational requirements.

Of the two models discussed in this chapter ray theory, or ray-theoretical solutions, chronologically preceed normal mode theory and was already in use during World War 2. It borrows much from its light theory counterpart which has been succesful in explaining the fundamental problems of optical instruments. Alternative wave-theoretical solutions were first reported by Pekeris [15] who used the normal mode solution of the wave equation to estimate the acoustic field of underwater explosions.

From a practical point of view the choice between ray theory and normal mode theory depends on the application. A rule of thumb would be do use ray theory with high frequencies in deep waters and normal mode theory for low frequencies in shallow waters [18].

4.1 Ray Theory

The essential basics of ray theory lie in the concept of wavefronts which were introduced in Sections 2.3 and 2.4. To arrive at the ray treatment of sound we must first

define the concept of a ray by utilising the geometrical concept of wavefronts. This can be done by employing a seventeeth century method used in optics. We then proceed to the differential equations of both wavefronts and ray paths. Ultimately, we get rather simple expressions to determine the path of a single ray and these expressions are later turned into a path tracing computer program in Section 7.1. Much of the theory presented in this section owes to [8].

4.1.1 Generalization of a Ray

Essentially a ray is the normal of a wavefront. To formulate the concept of a general ray we begin with a principle called Huygens' principle. This geometrical method for finding succesive wavefronts with time was originally established by the Dutch scientist Christian Huygens in 1678 [22]. The core of the principle is the assumption made by Huygens that every point of a wavefront may be considered the source of a secondary wavefront that spreads out in all directions with a speed equal to the speed of propagation of the wave [22]. An example of the Huygens' principle is given in Figure 4.1. First, the wavefront is drawn at time $t = 0$. The shape of the wavefront at time $t = dt$ is determined by drawing lines perpendicular to the original wavefront. The lines will have the length of cdt and if this process is repeated multiple times the wavefront can be constructed at any time t.

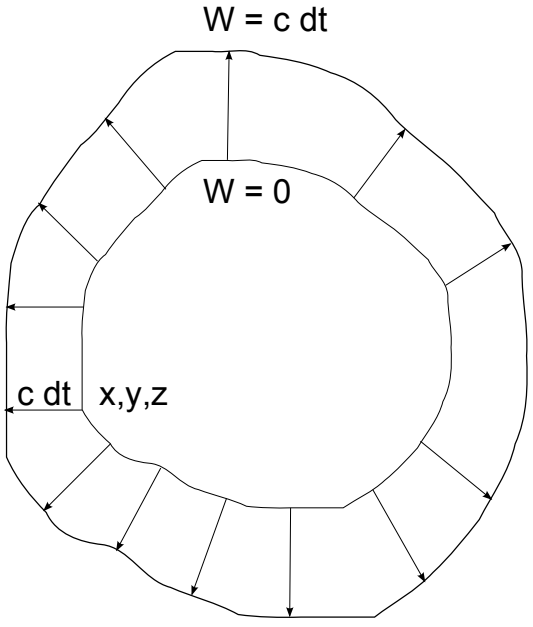

Figure 4.1: A demonstration of the Huygens' principle for constructing successive wavefronts. The initial wavefront expands by a length of cdt in the direction of the normal.

4.1.2 Eikonal Equation

In this section we derive the eikonal equation which is the fundamental equation of ray acoustics [8].

Let us start by considering one ray element from Figure 4.1 at any time t. Let this ray element be PP' and let the coordinates of P be (x, y, z). For a time interval of dt and for direction cosines α, β, γ of PP' the end point P' has the coordinates $(x + \alpha cdt, y + \beta cdt, z + \gamma cdt)$. The wavefront at time $t + dt$ is

$$W(x + \alpha cdt, y + \beta cdt, z + \gamma cdt) = c_0(t - t_0 + dt). \tag{4.1}$$

For a small cdt and by using equation (2.32) we have

$$\alpha\frac{\partial W}{\partial x} + \beta\frac{\partial W}{\partial y} + \gamma\frac{\partial W}{\partial z} = \frac{c_0}{c}. \tag{4.2}$$

Next, we eliminate the direction cosines α, β, γ. We start by stating two well known theorems of analytical geometry. The first defines the proportions of the directions cosines of a surface normal. For the surface W the proportions are

$$\alpha : \beta : \gamma = \frac{\partial W}{\partial x} : \frac{\partial W}{\partial y} : \frac{\partial W}{\partial z}. \tag{4.3}$$

The second theorem defines the sum of the squares of the direction cosines

$$\alpha^2 + \beta^2 + \gamma^2 = 1. \tag{4.4}$$

Using equations (4.3) and (4.4) we have,

$$\alpha = \left[\left(\frac{\partial W}{\partial x}\right)^2 + \left(\frac{\partial W}{\partial y}\right)^2 + \left(\frac{\partial W}{\partial z}\right)^2\right]^{-\frac{1}{2}} \frac{\partial W}{\partial x} \tag{4.5}$$

$$\beta = \left[\left(\frac{\partial W}{\partial x}\right)^2 + \left(\frac{\partial W}{\partial y}\right)^2 + \left(\frac{\partial W}{\partial z}\right)^2\right]^{-\frac{1}{2}} \frac{\partial W}{\partial y} \tag{4.6}$$

$$\gamma = \left[\left(\frac{\partial W}{\partial x}\right)^2 + \left(\frac{\partial W}{\partial y}\right)^2 + \left(\frac{\partial W}{\partial z}\right)^2\right]^{-\frac{1}{2}} \frac{\partial W}{\partial z} \tag{4.7}$$

Substituting equations (4.5), (4.6) and (4.7) into equation (4.2) and squaring both sides we have the eikonal equation,

$$\left(\frac{\partial W}{\partial x}\right)^2 + \left(\frac{\partial W}{\partial y}\right)^2 + \left(\frac{\partial W}{\partial z}\right)^2 = n^2(x, y, z), \tag{4.8}$$

where $n(x, y, z)$ is the index of refraction and is defined by

$$n(x, y, z) = \frac{c_0}{c(x, y, z)}. \tag{4.9}$$

The eikonal equation (4.8) defines the direction of the ray elements in respect to the local velocity of the wavefront which on the other hand is defined by the local index of refraction.

4.1.3 Rays in Vertical Velocity Gradients

In this section we examine the behaviour of ray paths in vertical velocity gradients. We start with the eikonal equation and use it to derive simple expressions to be used in a ray trace algorithm.

The eikonal equation (4.8) defined the direction cosines of a wavefront in regard to the index of refraction of the medium. Combining equations (4.8) and (4.5),(4.6),(4.7) yields

$$\alpha = \frac{1}{n}\frac{\partial W}{\partial x}; \quad \beta = \frac{1}{n}\frac{\partial W}{\partial y}; \quad \gamma = \frac{1}{n}\frac{\partial W}{\partial z}. \tag{4.10}$$

Now we eliminate W from the equations (4.10) using the formulas $\partial^2 W/\partial x \partial y = \partial^2 W/\partial x \partial y$, etc. The first equation of (4.10) is differentiated with respect to y and the second with respect to x. If this result is equated a relation between α, β, and n is obtained. Proceeding similarly with the rest of equation (4.10) we get,

$$\frac{\partial(n\alpha)}{\partial y} = \frac{\partial(n\beta)}{\partial x}; \; \frac{\partial(n\alpha)}{\partial z} = \frac{\partial(n\gamma)}{\partial x}; \; \frac{\partial(n\beta)}{\partial z} = \frac{\partial(n\gamma)}{\partial y}. \tag{4.11}$$

For a ray path of length s we can use the relationship of equation (4.11) to produce the changes of α, β, and γ along the ray path. We get,

$$\frac{d(n\alpha)}{ds} = \frac{\partial(n\alpha)}{\partial x}\frac{dx}{ds} + \frac{\partial(n\alpha)}{\partial y}\frac{dy}{ds} + \frac{\partial(n\alpha)}{\partial z}\frac{dz}{ds}. \tag{4.12}$$

If we assume that,

$$\frac{dx}{ds} = \alpha; \quad \frac{dy}{ds} = \beta; \quad \frac{dz}{ds} = \gamma, \tag{4.13}$$

equation (4.12) becomes

$$\frac{d(n\alpha)}{ds} = (\alpha^2 + \beta^2 + \gamma^2)\frac{\partial n}{\partial x} \tag{4.14}$$

and simplifies to

$$\frac{d(n\alpha)}{ds} = \frac{\partial n}{\partial x}.$$

If the same method is used for $d(n\beta)/ds$ and $d(n\gamma)/ds$ we have a set of three ordinary differential equations,

$$\frac{d(n\alpha)}{ds} = \frac{\partial n}{\partial x}; \quad \frac{d(n\beta)}{ds} = \frac{\partial n}{\partial y}; \quad \frac{d(n\gamma)}{ds} = \frac{\partial n}{\partial z}. \tag{4.15}$$

If the sound velocity is a function of y, also n depends only on y and equations (4.15) becomes,

$$\frac{d(n\alpha)}{ds} = 0; \quad \frac{d(n\beta)}{ds} = \frac{\partial n}{\partial y}; \quad \frac{d(n\gamma)}{ds} = 0 \tag{4.16}$$

and since we have $n\alpha = constant$ and $n\gamma = constant$ also $\frac{\gamma}{\alpha} = constant$. This can be interpreted as a condition which imposes the ray path to lie on a two dimensional plane. By taking this into account we can continue to solve the ray paths for the two dimensional case where the sound velocity continues to be a function of y only.

It is now important to agree with the convention of the direction of the y axis. As water depth increases downwards we also take the y axis positive downwards. The angle between a direction in the xy plane and the positive x axis is denoted by θ. The sign of θ is positive for a descending (y increases with x) ray and negative for a climbing ray. Using these relations we have

$$\alpha = \cos\theta; \quad \beta = \sin\theta; \quad \gamma = 0. \tag{4.17}$$

For a sound velocity dependent of y only and by using the relations in equation (4.17) equation (4.15) becomes

$$\frac{d(n\cos\theta)}{ds} = 0; \quad \frac{d(n\sin\theta)}{ds} = \frac{dn}{dy}. \tag{4.18}$$

For a ray path between points P and P', where P is located at depth where $c(y) = c_0$ and θ_0 being the direction of the ray, the first equation of (4.18) becomes

$$\frac{\cos\theta}{\cos\theta_0} = \frac{c}{c_0} \equiv \frac{1}{n}. \tag{4.19}$$

The form of equation (4.19) is identical to (2.39) introduced in Section 2.4. The second equation of (4.18) defines the curvature of the ray at any point. This curvature is defined by $d\theta/ds$ which we will now derive. From (4.18) we have

$$\frac{dn}{dy} = n\cos\theta\frac{d\theta}{ds} + (\sin\theta)^2\frac{dn}{dy} \tag{4.20}$$

and since $\sin\theta = dy/ds$ equation (4.20) becomes

$$\frac{d\theta}{ds} = \frac{1}{n}\frac{dn}{dy}\cos\theta = \frac{d(\log n)}{dy}\cos\theta. \tag{4.21}$$

By stating $\log n = \log c_0 - \log c$ equation (4.21) becomes

$$\frac{d\theta}{ds} = -\frac{d(\log c)}{dy}\cos\theta. \tag{4.22}$$

The behaviour of a ray between two layers of n can now be deduced from the equation (4.22). Consider a ray traveling towards the surface ($dy < 0$). If the new layer has a higher speed of sound then $\log c_0 - \log c > 0$ and the curvature $d\theta/ds$ has a positive sign and the ray is bent downward towards the bottom. If the layer has a lower speed of sound then the ray is bent upwards towards the surface. For a ray traveling towards the bottom ($dy > 0$) this behaviour is reversed. In a nutshell it can be said that a ray entering a layer of a lower speed of sound is bent away from the layer and a ray entering a layer of a higher speed of sound is bent towards the layer.

For a constant velocity gradient of a we have $c = c_0 + ay$ and for all points on the ray we have

$$\frac{d\theta}{ds} = -\frac{dc}{dy}\frac{\cos\theta_0}{c_0} = -\frac{a\cos\theta_0}{c_0},$$

where θ_0 is the initial angle of the ray and c_0 is the initial velocity of sound. In this type of velocity gradient the curvature of the ray is constant and the ray follows the arc of a circle. The radius of this circle is defined by

$$r = \left|\frac{c_0}{a\cos\theta_0}\right|. \tag{4.23}$$

The new angle θ_1 at which the ray leaves the layer is defined by

$$\theta_1 = \arccos\left(\frac{c\cos\theta_0}{c_0}\right). \tag{4.24}$$

The horizontal range along the x axis which the ray travels in the layer is defined by

$$range = h\cot\frac{1}{2}(\theta_0 + \theta_1), \tag{4.25}$$

where h is the thickness of the layer. Equations (4.23), (4.24), (4.25) are simple yet accurate expressions which can be easily implemented to produce a ray tracing algorithm.

4.2 Normal Mode Theory

In this section the expression for the normal modes used by KRAKEN are presented. The complete derivation of the transmission loss from the normal mode model can be found in [16].

We start by rewriting the wave equation (2.19) as

$$\nabla\left(\frac{1}{\rho}\nabla P\right) - \frac{1}{\rho c^2(z)}P_{tt} = -s(t)\frac{\delta(z-z_s)\delta(r)}{2\pi r}, \tag{4.26}$$

where $P(r,z,t)$ is the acoustic pressure function of depth z, range r and time t, $s(t)$ is the acoustic point source, $\rho(z)$ is the density and $c(z)$ is the sound velocity. For the surface, where $z=0$ and bottom, where $z=D$ we have $P(r,0,t) = P_z(r,D,t) = 0$. For a harmonic source we have $s(t) = e^{-i\omega t}$ and $P(r,z,t) = p(r,z)e^{-i\omega t}$. After substituting these into equation (4.26) and separating variables and solving the resulting classical Sturm-Liouville eigenvalue problem we have

$$p(r,z) = \frac{i}{4\rho(z_s)}\sum_{m=1}^{\infty} Z_m(z_s)Z_m(z)H_0^{(1)}(k_m r),$$

where Z_m is the mode shape function, k_m the horizontal propagation constant and $H_0^{(1)}$ the Hankel function of the first kind. Now the transmission loss can be written as

$$TL(r,z) = -20\log_{10}\left|\frac{p(r,z)}{p^0(r=1)}\right|,$$

where $p^0 = \frac{e^{ik_0 r}}{4\pi r}$. For shallow water cases where the bottom interaction is dominant and the bottom properties poorly known, it is more appropriate to use the incoherent transmission loss

$$TL^{inc}(r,z) \approx -20\log_{10}\frac{1}{\rho(z_s)}\sqrt{\frac{2\pi}{r}}\sqrt{\sum_{m=1}^{\infty}\left|\frac{Z_m(z_s)Z_m(z)}{\sqrt{k_m}}\right|}.$$

5. MULTIPATH PROPAGATION

Multipath propagation of underwater sound sources is almost unavoidable. Whether the source and the hydrophone are situated in deep or shallow water the propagation path of the acoustic energy is bound to be interrupted by the surface, bottom or some obstacle. This property of underwater sound imposes not only a problem but also presents possibilities of advanced target parameter detection. By studying the results of numerical models, such as the ray theory, it can be shown that certain real life interference patterns can be linked to specific target parameters. These parameters include the speed and depth of the source and provide useful information for the detection and classification of the target. Some previous work on underwater interference patterns in target recognition can be found in [19] which however considers only the so called Lloyd's mirror, or the surface reflection and also disregards the effects of refraction. These simplifications lead to interesting theoretical interference patterns but their use in real situtations can be disputed. For instance, the surface reflection does not always become the dominant factor of the interference pattern and in some scenarios it may be almost canceled out by other propagation paths. For more reliable models the multiple bottom and surface reflections should be taken into account. Also, the variation in the sound propagation paths caused by refraction may need to be included and often the temperature profile of shallow seas such as the Baltic Sea can be modeled quite accurately to give more realistic refraction patterns of acoustic energy.

In this chapter the basics of multipath propagation are presented. These include the properties of bottom and surface reflections, the time delays imposed by the path differences, and the variations in these delays under different temperature profiles.

5.1 Phase Change at the Boundaries

The behaviour of a sound wave when it meets the interface of two media can be expressed using the characteristic acoustic impedances of the media. The acoustic impedance is denoted by z and is equal to the ratio of the acoustic pressure p in the media to the associated particle speed u as $z = p/u$. For plane waves this ratio becomes $z = c\rho$, where c is the wave speed and ρ the density of the medium. The acoustic impedance is a real or complex quantity depending on the viscoelastic properties of the medium and in our case it suffices to assume that it is real.

The reflection coefficient characterizing the amplitude change at the interface is

$$R = \frac{A_r}{A_i}, \tag{5.1}$$

where A_r and A_i are the reflected and incident amplitudes (2.33)-(2.35).

For plane waves, the reflection coefficient R can be related to the acoustic impedances of the propagation media by

$$R = \frac{z_2 - z_1}{z_2 + z_1} = \frac{c_2\rho_2 - c_1\rho_1}{c_2\rho_2 + c_1\rho_1}. \tag{5.2}$$

In this work the seabed is modeled as a substance with a flat surface in which the acoustic impedance is much higher than that of seawater. Thus $z_2 >> z_1$ implying $R \sim 1$ at the seawater-bottom interface. On the other hand, the acosutic impedance of air is much smaller than that of seawater, i.e. at the seawater-air interface $z_2 << z_1$ implying $R \sim -1$.

Thus seawater-bottom interface induces zero phase change while the seawater-air interface induces a phase change of π radians [12].

5.2 Ideal Model for Multipath Delays

An ideal model for multipath propagation is presented in [12]. This model considers the sound velocity constant at every depth thus disregarding the effects of refraction. The multiple surface and bottom reflected paths are considered to correspond to image sources located horizontally at the source and vertically below and above the depth of the source. This simplification is possible since the reflections at both boundaries are considered specular.

Following four types of fundamental reflection paths are considered: paths which are first and last reflected by the surface, denoted with S and paths which are first and last reflected by the bottom, denoted with B, paths which are first reflected by surface and then by bottom, denotes with SB, and finally paths which are reflected first by bottom and then by surface, denoted with BS. The length of the paths can be computed as:

$$\begin{cases} L_S = \sqrt{D^2 + (2(i-1)H + z_t + z_r)^2} \\ L_B = \sqrt{D^2 + (2iH - z_t - z_r)^2} \\ L_{SB} = \sqrt{D^2 + (2iH + z_t - z_r)^2} \\ L_{BS} = \sqrt{D^2 + (2iH - z_t + z_r)^2}, \quad \text{where } i = 1, 2, 3, ... \end{cases} \tag{5.3}$$

and where D is the horizontal distance from the transmitter to receiver, z_t and z_r the transmitter and receiver depths, and H the depth of the water body. The running

number i denotes the number of consecutive reflections. For H, z_t, and z_r the depths are considered positive.

The time delay d corresponding to each path is the difference between the direct path length and the reflected path length divided by the speed of sound

$$d = \frac{L_{path} - L_{direct}}{c}, \tag{5.4}$$

where c denotes the speed of sound and L_{direct} is defined as

$$L_{direct} = \sqrt{D^2 + (z_r - z_t)^2}.$$

Let us consider a case in which $H = 30$ m, $D = 250$ m, $z_t = 12$ m, and $z_r = 20$ m. For the speed of sound we have $T = 16.4\,°\mathrm{C}$, $S = 2.27$ ppt, and pressure is one atmosphere. With these parameters equation (3.3) equals 1469 m/s. The corresponding time delays for L_S, L_B, L_{SB}, L_{BS} where $i = 1, 2$ are shown in Table 5.1.

path	S	SBS	B	BSB	SB	SBSB	BS	BSBS
d_{ideal}	0.0014	0.0112	0.0011	0.0102	0.0036	0.0163	0.0062	0.0210

Table 5.1: Multipath delays in ideal model.

5.3 Refraction and Multipath Delays

When refraction is present the ideal multipath propagation model given by equation (5.3) no longer holds. Let us consider the same scenario as in Section 5.2 with a realistic sound speed profile that changes according to depth. For proper values of T and S we use [9] and the speed profile computed with equation (3.3) is given in Table 5.2. Further, this profile is interpolated to obtain a continuous profile.

We then compute the delays for the same paths as we did in Section 5.2 this time using the ray tracer from Section 7.1.1 and the interpolated profile. Values for L_{path} and L_{direct} in equation (5.4) are replaced with the corresponding values given by the ray trace algorithm. The computed time delays with refraction taken into account are shown in Table 5.3. The differences between the ideal model and the refracted model are shown in Table 5.4 where Δd is equal to $d_{refr.} - d_{ideal}$.

Depth, m	Temperature, °C	Salinity, ppt	Speed of sound, m/s
0	16.4	2.27	1469
10	14.0	1.68	1460
20	7.7	2.56	1441
30	5.9	3.33	1435

Table 5.2: A realistic sound speed profile with depth, temperature, and salinity.

path	S	SBS	B	BSB	SB	SBSB	BS	BSBS
$d_{refr.}$	0.0006	0.0112	0.0024	0.0110	0.0038	0.0163	0.0065	0.0216

Table 5.3: Multipath delays in the refracted model.

path	S	SBS	B	BSB	SB	SBSB	BS	BSBS
Δd	−0.0008	0.0000	0.0013	0.0008	0.0002	0.0000	0.0003	0.0006

Table 5.4: Difference in multipath delays between the refracted and the ideal model.

6. COMPUTING INTERFERENCE PATTERNS

The effects of a multipath environment can be examined by studying the spectrum of the received signal. Previous work for both terrestial [11] and underwater [19] cases show that the existence of delayed replica, such as the underwater surface or bottom reflections can be linked to prominent patterns in the spectrum. Further, for a moving vehicle, such as submersible, these patterns have been proven to vary over time. Using time-frequency analysis a detailed view of the spectral signature left by the submersible and its specific multipath environment emerges. In this chapter the basic signal processing theory for this type of time-frequency analysis is presented.

6.1 Analog to Digital Conversion

Before any type of digital signal processing can be applied to a sound recording the sound information has to be converted to a digital form. Usually this process begins with a transducer which converts the sound energy, or pressure variations into electric energy [1]. For underwater cases these transducers are called hydrophones and they use piezoelectric effect in which certain materials when subjected to pressure or stress accumulate charge [18]. After being transduced into electricity the signal is often amplified or compensated for any nonlinearities in the transducer and these operations are called signal conditioning [1]. Signal conditioning is followed by an analog low-pass filter which removes any high frequency noise generated by the transducer but also more importantly prevents the aliasing of higher frequencies to lower frequencies during the analog to digital (A/D) conversion.

The cut-off frequency of the analog low-pass filter is defined by the sampling frequency, f_s, of the A/D converter. Determining a proper f_s is important since it defines the highest frequency the A/D converter is able to digitize. This frequency is known as the Nyquist frequency [1] and is half the sampling rate of the discrete signal. That is $f_N = f_s/2$ where f_s is the sampling rate. The choice of f_s depends both on the frequency range of interest and on the choice of A/D converter. Two types of A/D converters are generally used [14]. The first one is known as sample-and-hold and it operates at the sampling rate of f_s. The second and usually preferred converter is known as sigma-delta A/D converter and it operates at a high multiple of f_s. The benefits of a sigma-delta A/D converter over sample-and-hold are the simpler analog filter hardware and the reduction of quantization noise [14].

6.2 Discrete Fourier Transform

Spectral analysis which means the representation of a signal by its frequency content is performed using the Fourier transform. In brief, the Fourier transform transforms a signal from time-domain to frequency-domain. However depending on how the time-domain signal is represented there are several conceptually different forms of the Fourier transform. For analog signals Fourier methods include continuous-time Fourier transform (CTFT) for non-periodic signals and continuous-time Fourier series (CTFS) for periodic signals. In digital or discrete systems the counterparts are the discrete-time Fourier series (DTFS) and discrete-time Fourier transform (DTFT). These transforms produce continous frequency spectra which on the other hand implies infinite length. Using a digital computer the spectrum can be computed only at a finite number of points and this leads to the discrete Fourier transform (DFT) which corresponds to equally spaced sampling of the DTFT spectrum.

We will use the following notation in explaining the emergence of the interference phenomena. We denote the sound signal received at the hydrophone by $x(t)$, where t denotes time and the corresponding sampled digital signal by $x(n)$. We denote the sampling frequency by f_s Hz, where the sampling interval $T = \frac{1}{f_s}$.

The Fourier transform of $x(t)$ is

$$X(\omega) = \int_{-\infty}^{\infty} e^{-i\omega t} x(t) dt \tag{6.1}$$

and we can formally recover $x(t)$ from $X(\omega)$ by

$$x(t) = \frac{1}{2\pi} \int_{-\infty}^{\infty} e^{iwt} X(\omega) dw. \tag{6.2}$$

We denote the relation between the signal and its Fourier transform by $x(t) \sim X(\omega)$.

The Fourier transform is linear and the Fourier transform of a signal and its delayed version obey the relation

$$s(t) \sim X(\omega) \;\; if \; and \; only \; if \;\; s(t-d) \sim e^{-i\omega d} X(\omega). \tag{6.3}$$

This implies, that if $y(t)$ is the sum of $x(t)$ and delayed and attenuated (possibly with a phase shift of π) versions of $x(t)$, we have the following relation between the signals and their spectra. If,

$$y(t) = x(t) + A_1 x(t-d_1) + \ldots + A_k x(t-d_k) \tag{6.4}$$

then

$$Y(\omega) = (1 + A_1 e^{-i\omega d_1} + \ldots + A_k e^{-i\omega d_k}) X(\omega) \tag{6.5}$$

and $A_i > 0$ if there is a 0 phase shift and $A_i < 0$ if there is a phase shift of π. The formulas (6.4) and (6.5) allow us to examine the spectrum of the corresponding multipath signal if we know the spectrum of the original signal.

In practice we work with the digital (sampled) signals and have only a section of finite length N of the signal $x(n)$ available. The DFT of $x(n)$ is defined as

$$X_d(m) = \sum_{n=0}^{N-1} x(n) e^{-i2\pi mn/N}. \tag{6.6}$$

for $m = 0, 1, \ldots, N-1$, where integer n denotes time instant or time index and integer m denotes discrete frequency or frequency index. $X_d(m)$ gives the frequency, amplitude and phase response of the input signal $x(n)$ at N equally spaced frequencies.

As in the continuous case, we can recover $x(n)$ from its DFT via

$$x(n) = \frac{1}{N} \sum_{m=0}^{N-1} X_d(m) e^{\frac{i2\pi mn}{N}}. \tag{6.7}$$

The linearity and delay formulas hold for DFT and we have a relation corresponding to (6.4) and (6.5) above.

6.3 Fast Fourier Transform

The direct numerical computation of equation (6.6) for each m requires N complex multiplications and $(N-1)$ complex additions [1]. Computing $X_d(n)$ over all of $m = 0, 1, \ldots, N-1$ requires N^2 complex multiplications and $N(N-1)$ complex additions. As N increases the computational requirements of equation (6.6) increase as well. The computation time for the traditional numerical DFT is proportional to N^2. Thus a more efficient approach for computing the DFT is required. One such approach is the Cooley-Tukey algorithm [3]. The Cooley-Tukey type of recursive fast Fourier transform (FFT) algorithms have best efficiency when N is a power of two. In these cases when $N = 2^p$ the computational time is approximately proportional to $2Np$. Also other types of FFT algorithms exist and for example Matlab uses a combination of Cooley-Tukey and other independent implementations for computing the DFT [13].

6.4 Time-frequency Analysis

DFT provides tools to analyse a signal by its frequency and amplitude yet it provides these results over the whole signal $x[n]$. Therefore, DFT works best for stationary signals where the frequency-amplitude response remains largely constant. For non-stationary signals, such as recordings from a hydrophone, DFT is not an effective

tool for analysis. In cases where it is necessary to analyse small portions of a signal we use a modified version of DFT called short-time Fourier transform or STFT. To further analyse the results of STFT's we use spectrograms which map the results of individual STFT's over a longer time span.

6.4.1 Short-Time Fourier Transform

In essence the STFT restricts the frequency analysis of a signal over some particular interval. The extraction of an interval of length L is achieved by multiplying the original signal $x(n)$ with a truncation function which has the value 1 over the interval of interest and is zero otherwise. Truncation functions are usually referred as window functions since the effect corresponds to viewing the signal through a window. There exists many types of window functions and the truncation function mentioned previously is known as a rectangular window for its shape. The shape of the window function distorts the shape of the signal and therefore creates unwanted artifacts to the spectrum. A rectangular window has the most prominent discontinuities and is less suitable for time-frequency analysis unless the length of the window L is a true period of $x(n)$ [17]. Since usually the true period of the signal is unknown, more smoother window functions such as Hann window or Gaussian window can be used to achieve a better correspondance with the original spectrum.

6.4.2 Interference Patterns on Spectrogram

STFT of some length over the whole of any signal results in the complex spectrum representation of the signal. A spectrogram is a power spectrum of the complex spectrum. A spectrogram contains all the STFT power spectras and is represented as an image with both time and frequency axes. Unlike a single DFT over the whole signal, the spectrogram now contains the time-localized spectras and can be used to analyse the frequency distribution with time. In most cases the horizontal axis represents time and the vertical axis contains the frequency content of that specific time frame.

The synthetic spectrograms in this work are generated from the time-of-flight, amplitude, and phase information gathered from rayTrace or the ideal model. For the third party models the transmission loss information can be directly turned into the same kind of images without computing the complex spectrum. The time delays are computed from the time-of-flight information by subtracting the direct path's time-of-flight from the other paths. The synthetic spectrograms have a time sampling of 1 second and the width of the frequency bins is 1 Hz. A spectrogram with a time span of t_s and a frequency range of 1 to f_e would have the dimensions $f_e \times t_s$. The time delay and the amplitude information for the many paths are

stored in matrices. If the number of paths found is N_p then both the time delay and amplitude matrices would have dimensions $N_p \times t_s$. The phase information can be stored using a single value for each path. Thus, the vector containing the phase information has a length of N_p.

The pseudocode for spectrogram synthetization is given in Algorithm 1. The spectrogram synthetization begins with creating a complex spectrum matrix having the value 1 for each element. Each row is then element-wise multiplied by the direct path amplitude vector. This ensures that the complex spectrum is initialized to a reasonable amplitude level. After this, each time instant, each frequency bin, and each path (excluding the direct path) are looped through. The frequency domain modification of the complex spectrum is performed with the corresponding phase, amplitude, and time delay information. Finally, the magnitude of the complex spectrum is squared to produce the power spectrum, or spectrogram.

input : delays T_D, amplitudes A of size $N_p \times t_s$
input : phases ϕ of size N_p
output: power spectrum P of size $f_e \times t_s$
create an array of dimensions $f_e \times t_s$ *as* S
initialize each element in S *with* 1
multiply each row in S *element-wise with* $A(1,:)$
for $f \leftarrow 1$ **to** f_e **do**
  for $t \leftarrow 1$ **to** t_s **do**
    for $p \leftarrow 2$ **to** N_p **do**
      $S(f,t) = S(f,t) + A(p,t) \cdot e^{-i(T_D(p,t)\cdot f \cdot 2\cdot\pi + \phi(p))}$
    end
  end
end
$P(f,t) = |S(f,t)|^2$

Algorithm 1: Spectrogram synthetization.

6.4.3 Lloyd's Mirror Effect

Interference by the direct and the surface reflected underwater sound fields is known as the Lloyd's mirror effect. This effect is a special case of multipath propagation and is unique to surface reflections. Further, the Lloyd's mirror effect is specifically restricted to those propagation paths which are only once reflected by the surface before reaching the sensor. The Lloyd's mirror effect is considered to be useful for distinguishing between submerged and surface ships since the interference pattern it creates should only be detectable for submerged vessels. The use of Lloyd's mirror effect has been previously discussed in [11] and [19].

We assume that the target moves on a straigth line at a constant speed v at depth D_1, and that the hydrophone is at depth D_2. We also assume that the target

makes its closest point of approach to the sensor at time instant τ_c and at that time the horizontal distance between the target and the sensor is D_c. The direct range between the target and the sensor at τ_c becomes $R_D = \sqrt{D_c^2 + (D_2 - D_1)^2}$ and the surface reflected range becomes $R_S = \sqrt{D_c^2 + (D_2 + D_1)^2}$. The time variation of the nth destructive interference frequency is defined as

$$f_n(t) \cong \left(\frac{n}{2}\right)\left(\frac{c}{D_1 D_2}\right) \times \overline{R}(t), \quad n = 1, 2, 3, \ldots \tag{6.8}$$

where c is the speed of sound and where $\overline{R}(t)$ is defined as

$$\overline{R}(t) = \left(\sqrt{R_D^2 + v^2(\tau_d(t) - \tau_c)} + \sqrt{R_S^2 + v^2(\tau_s(t) - \tau_c)}\right)/2,$$

where $\tau_d(t)$ and $\xi_d(t)$

$$\tau_d(t) = \frac{c^2 t - v^2 \tau_c - \xi_d(t)}{c^2 - v^2}, \; \xi_d(t) = \sqrt{R_D^2(c^2 - v^2) + v^2 c^2 (t - \tau_c)^2},$$

and $\tau_s(t)$ and $\xi_d(t)$

$$\tau_s(t) = \frac{c^2 t - v^2 \tau_c - \xi_s(t)}{c^2 - v^2}, \; \xi_s(t) = \sqrt{R_S^2(c^2 - v^2) + v^2 c^2 (t - \tau_c)^2}.$$

Using the following parameters: $v = 5$ m/s, $\tau_c = 300$ s, $D_c = 150$ m, $D_1 = 12$ m, $D_2 = 24$ m, $c = 1469$ m/s, and $n = 1, 2, 3, 4, 5$, the equation (6.8) yields the interference pattern in Figure 6.1.

As in [19] we can write the path length difference between the direct and surface reflected signals as

$$\Delta L(t) = \frac{2 D_1 D_2}{\overline{R}(t)},$$

and from this we can write the time delay between the two paths as

$$delay(t) = \frac{\Delta L(t)}{c}. \tag{6.9}$$

Using the same parameters as in Figure 6.1 we can compute the spectrogram of the interference pattern by using equation (6.9) and Algorithm 1. The result is shown in Figure 6.2. In coming chapters we examine the effects of multipath environments under similar parameters. In this work the focus is on the effects of different sound speed profiles and on the effects of refraction. Because of this, the exact formulas of equations (6.8) and (6.9) are not used.

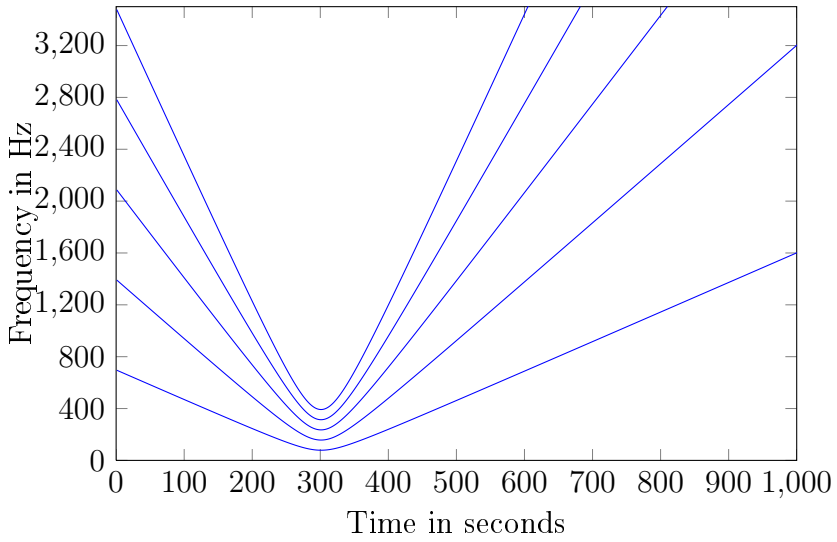

Figure 6.1: Interference pattern for Lloyd's mirror phenomenon for a passing submarine example.

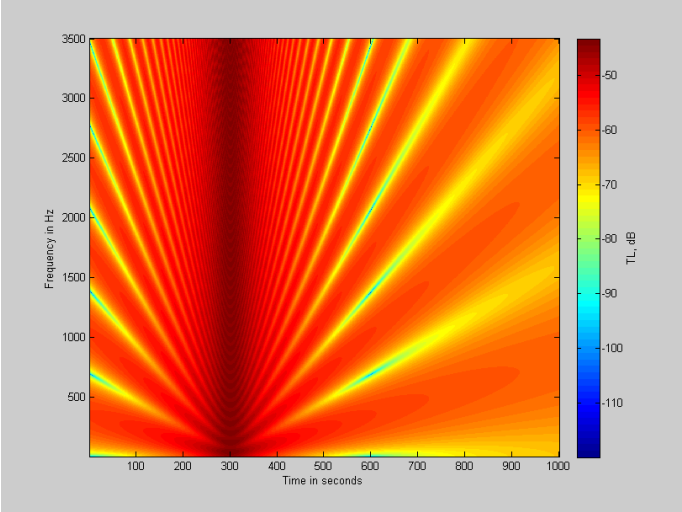

Figure 6.2: Spectrogram for Lloyd's mirror phenomenon for a passing submarine example.

7. NUMERICAL COMPUTATION OF THE ACOUSTIC FIELD

In this work three numerical methods for computing underwater acoustic fields are presented. The Matlab version is a ray tracing algorithm developed by the author. KRAKEN and BELLHOP are the work of Michael B. Porter who began to work on the KRAKEN normal mode program in the early 1980's as a part of his dissertation [16]. Both KRAKEN and the BELLHOP ray tracing program are part of a wider package referred as the Acoustics Toolbox also developed by Porter. In addition to normal mode and ray tracing methods the Acoustics Toolbox also includes fast field progam models SCOOTER and SPARC but they are not discussed in this work.

While the author's ray tracing implementation is fully developed and executed from the Matlab environment, KRAKEN, BELLHOP, and FIELD have been compiled from Fortran 90 source code into 32-bit Windows binaries. The latter of the three is used to compute the acoustic field from the modes calculated by KRAKEN. The Acoustics Toolbox offers both the precompiled binaries and the source code with the notion that the user will probably need to recompile the source. Since not all of the needed features could be found in The Acoustics Toolbox it was necessary to be able to work from the Matlab environment. Matlab functions to read the output files of the programs are available online and the decent specification allowed the developement of Matlab functions to generate all necessary input files.

7.1 Matlab

Matlab environment (version 7.13.0.564 (R2011b)) was used for the ray tracing algorithm. The behaviour of acoustic rays is limited to a number of specific cases (see Section 4.1.3) and the design emphasis was to divide the algorithm to deal with each case separately. This approach made the algorithm easy to both develop and debug.

The algorithm is implemented in a Matlab function rayTrace which traces the path of a single ray over a specific horizontal range starting with a specific initial angle. In this section the separate cases for ray behaviour between adjacent layers of media are presented.

7.1.1 The Ray Trace Algorithm

The function rayTrace computes the propagation of acoustic rays by dividing the ray tracer to four cases: a ray traveling upwards/downwards and the temperature gradient being positive/negative. The reflections at the boundaries are always considered specular. For specular reflections, $\theta_r = -\theta_i$ where θ_r and θ_i are the angles of the reflected and incident rays.

The execution of the algorithm is similar to generic ray tracers. A starting point given as a x, y pair is selected and a complete ray path is traced in segments. Each segment has a starting point and an ending point and each ending point functions as a starting point for the next ray segment. The medium, which in this case is a body of seawater, is divided vertically into layers. Each layer has its own index of refraction and the behaviour in and between each pair of layers is determined using expressions derived from Snell's law given in Section 2.4. After a ray segment has reached a specified termination line the execution is terminated. The termination line is a specific horizontal distance. The output values of rayTrace are the coordinates of the ending points of each ray segment, the total time-of-flight of the complete ray, the total distance traveled by the ray (the sum of the distances of each ray segment), and the phase of the complete ray. The phase of a ray is determined by the number of surface reflections in the ray path. An odd number of surface reflections results in a phase change of π radians. Zero, or an even number of surface reflections, result in zero phase change as explained in Section 5.1.

Variables Used in Cases I-IV

The variables used by the algorithm are presented in Table 7.1.

Number of layers.	n
Running number for the current layer.	l
Current angle in radians.	θ_1
Next angle in radians.	θ_2
Temperature gradient between the current and the next layer.	g
The radius of the ray segment computed in the current iteration.	r
N x 2 sized matrix containing layer depths and sound speeds.	$\boldsymbol{M}$
Horizontal displacement for a ray segment.	dx
The time-of-flight for a ray segment.	t
Length of the currently computed ray segment.	d
Phase at the next x,y point.	ϕ
Current x coordinate.	x_i
Current y coordinate.	y_i
Next x coordinate.	x_{i+1}
Next y coordinate.	y_{i+1}

Table 7.1: Variables used in rayTrace.

About the Angles and Layers

Layer matrix $\boldsymbol{M}$ contains the layer depths and sound velocities at the beginning of each layer.

$\boldsymbol{M}(:,1)$	$\boldsymbol{M}(:,2)$
0	1477
5	1470
12	1465

Table 7.2: Sound velocity matrix $\boldsymbol{M}$.

Current angle	Current layer	Next layer	Next depth	Next speed of sound
$\theta_1 > 0$	l	$l+1$	$\boldsymbol{M}(l+1,1)$	$\boldsymbol{M}(l+1,2)$
$\theta_1 < 0$	l	$l-1$	$\boldsymbol{M}(l-1,1)$	$\boldsymbol{M}(l-1,2)$

Table 7.3: Indexing the sound velocity matrix $\boldsymbol{M}$.

General Expressions

The following expressions are used in all four cases to compute the propagation of a sound ray for adjacent layers i, j, velocities c_i, c_j, depths D_i, D_j, and angles θ_i, θ_j. For the expressions in this section the ray travels from layer i to layer j.

Gradient

The gradient of sound velocity between two adjacent layers is

$$g_i = \frac{c_i - c_j}{D_i - D_j}.$$

Arc Radius

As in equation (4.23) the arc radius for the circular curvature of a ray in a vertical gradient is

$$r_i = \frac{c_i}{g_i \cdot |\cos(\theta_i)|}.$$

Angle of a Ray

The new angle for a ray is given by equation (4.24). For a ray bending back between adjacent layers the new angle becomes

$$\theta_j = -\theta_i,$$

and for a ray traveling through to the next layer it is

$$\theta_j = \arccos\left(\frac{c_j \cos\theta_i}{c_i}\right)$$

and for a ray reaching a boundary it becomes

$$\theta_j = -\arccos\left(\frac{c_j \cos\theta_i}{c_i}\right).$$

Arc Length

From trigonometry the length of a circular arc for a ray becomes

$$d_i = r_i \cdot (\theta_i - \theta_j).$$

Horizontal Displacement

The horizontal displacement for a ray is given by equation (4.25). For a ray bending back due to strong gradient between adjacent layers the horizontal displacement becomes

$$dx_i = \frac{2 \cdot c_i \cdot \sin(\theta_i)}{g_i \cdot \cos(\theta_i)},$$

and for a ray traveling through it is

$$dx_i = (D_i - D_j) \cdot \cot\left(\frac{\theta_i + \theta_j}{2}\right).$$

Time of Flight

The time of flight for a ray bending back between adjacent layers is

$$t_i = 2 \cdot (1/g_i) \cdot \left|\ln(\tan(\pi/4 - \theta_i/2))\right|,$$

and for a ray traveling through it is [12]

$$t_i = (1/g_i) \cdot \left|\ln\left(\frac{\tan(\pi/4 - \theta_j/2)}{\tan(\pi/4 - \theta_i/2)}\right)\right|.$$

Case I

The ray is traveling towards the bottom and the speed of sound increases. This is a typical situtation during the winter in high latitude regions. The signs for the ray angle and the sound speed gradient are given in Table 7.4.

Angle θ_1	Change in the speed of sound $\boldsymbol{M}(l+1,2) - \boldsymbol{M}(l,2)$
POSITIVE	POSITIVE

Table 7.4: Values of θ_1 and g in case I.

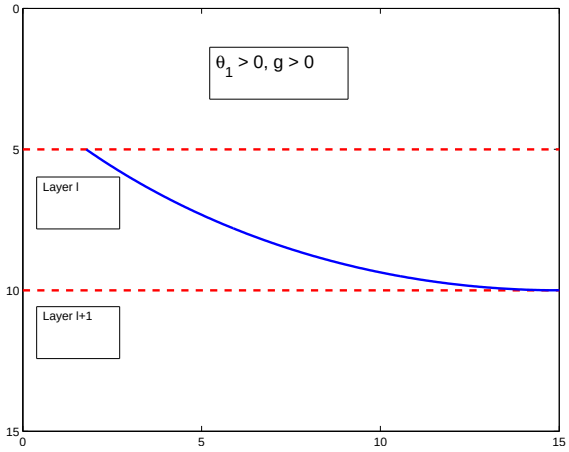

Figure 7.1: Ray behaviour in case I.

First the program computes values for the two variables given in Table 7.5.

Variable	Value
g	$(\boldsymbol{M}(l+1,2) - \boldsymbol{M}(l,2))/(\boldsymbol{M}(l+1,1) - \boldsymbol{M}(l,1))$
r	$(\boldsymbol{M}(l,2))/(g \cdot \cos\theta_1)$

Table 7.5: Expressions for g and r in case I.

After computing the values in Table 7.5 the algorithm proceeds to examine which of the three possibilities given in Tables 7.6-7.8 evaluates. If the ray is bend back by the sound speed gradient the values in Table 7.6 are computed. If the ray intersects bottom the values in Table 7.7 are computed. If the ray continues to the next layer the values in Table 7.8 are computed.

$\boldsymbol{M}(l+1,2) \cdot \cos\theta_1 > \boldsymbol{M}(l,2)$	
θ_2	$-\theta_1$
dx	$(2 \cdot \boldsymbol{M}(l,2) \cdot \sin\theta_1)/(g \cdot \cos\theta_1)$
t	$t + 2 \cdot 1/g \cdot \lvert \ln(\tan(\pi/4 - \theta_1/2)) \rvert$
d	$r \cdot 2 \cdot \theta_1$
l	l
ϕ	ϕ

Table 7.6: Rest of the variables for case I when ray bends back.

$l = n - 1$	
θ_2	$-\arccos(\boldsymbol{M}(l+1,2)/\boldsymbol{M}(l,2)) \cdot \cos(\theta_1)$
dx	$(\boldsymbol{M}(l,1) - \boldsymbol{M}(l+1,1)) \cdot \cot((\theta_1 + \theta_2)/2)$
t	$t + 1/g \cdot \lvert \ln(\tan(\pi/4 - \theta_2/2)/\tan(\pi/4 - \theta_1/2)) \rvert$
d	$r \cdot (\theta_1 + \theta_2)$
l	$l + 1$
ϕ	ϕ

Table 7.7: Rest of the variables for case I when next layer is bottom.

else	
θ_2	$\arccos(\boldsymbol{M}(l+1,2)/\boldsymbol{M}(l,2)) \cdot \cos(\theta_1)$
dx	$(\boldsymbol{M}(l,1) - \boldsymbol{M}(l+1,1)) \cdot \cot((\theta_1 + \theta_2)/2)$
t	$t + 1/g \cdot \lvert \ln(\tan(\pi/4 - \theta_2/2)/\tan(\pi/4 - \theta_1/2)) \rvert$
d	$r \cdot (\theta_1 + \theta_2)$
l	$l + 1$
ϕ	ϕ

Table 7.8: Rest of the variables for case I when ray continues to the next layer.

Case II

The ray is traveling towards the bottom and the speed of sound decreases. This is the most common vertical gradient in seawater and is usually found in almost all regions from spring to autumn excluding exceedingly high latitude regions. The signs for the ray angle and the sound speed gradient are given in Table 7.9.

Angle θ_1	Change in the speed of sound $\boldsymbol{M}(l+1,2) - \boldsymbol{M}(l,2)$
POSITIVE	NEGATIVE

Table 7.9: Values of θ_1 and g in case II.

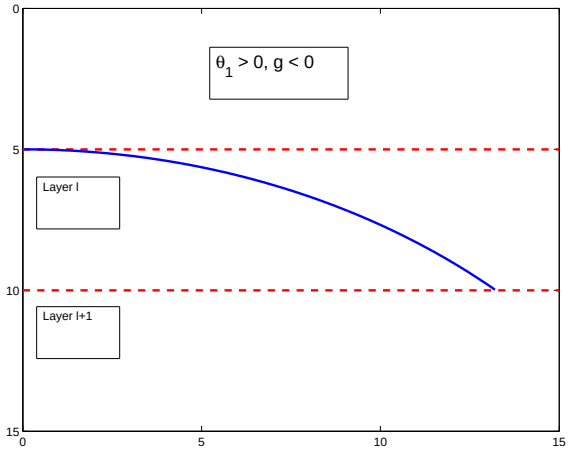

Figure 7.2: Ray behaviour in case II.

In case II the algorithm only needs to determine whether the ray intersects the bottom or continues to the next layer. If the ray intersects the bottom the values in Table 7.10 are computed. If the ray continues to the next layer values in Table 7.11 are computed.

$l = n - 1$	
g	$(\boldsymbol{M}(l+1,2) - \boldsymbol{M}(l,2))/(\boldsymbol{M}(l+1,1) - \boldsymbol{M}(l,1))$
r	$-(\boldsymbol{M}(l,2))/(g \cdot \cos\theta_1)$
θ_2	$-\arccos(\boldsymbol{M}(l+1,2)/\boldsymbol{M}(l,2)) \cdot \cos(\theta_1)$
dx	$(\boldsymbol{M}(l,1) - \boldsymbol{M}(l+1,1)) \cdot \cot((\theta_1 + \theta_2)/2)$
d	$r \cdot (\theta_1 + \theta_2)$
t	$t - 1/g \cdot \lvert \ln(\tan(\pi/4 - \theta_2/2)/\tan(\pi/4 - \theta_1/2)) \rvert$
l	$l + 1$
ϕ	ϕ

Table 7.10: Rest of the variables for case II when next layer is bottom.

else	
g	$(\boldsymbol{M}(l+1,2)-\boldsymbol{M}(l,2))/(\boldsymbol{M}(l+1,1)-\boldsymbol{M}(l,1))$
r	$-(\boldsymbol{M}(l,2))/(g\cdot\cos\theta_1)$
θ_2	$\arccos(\boldsymbol{M}(l+1,2)/\boldsymbol{M}(l,2))\cdot\cos(\theta_1)$
dx	$(\boldsymbol{M}(l,1)-\boldsymbol{M}(l+1,1))\cdot\cot((\theta_1+\theta_2)/2)$
d	$r\cdot(\theta_1+\theta_2)$
t	$t-1/g\cdot\lvert\ln(\tan(\pi/4-\theta_2/2)/\tan(\pi/4-\theta_1/2))\rvert$
l	$l+1$
ϕ	ϕ

Table 7.11: Rest of the variables for case II when ray continues to the next layer.

Case III

The ray is traveling towards the surface and the speed of sound decreases. This is the same situation as in case I except for the direction of the ray. The signs for the ray angle and the sound speed gradient are given in Table 7.12.

Angle θ_1	Change in the speed of sound $\boldsymbol{M}(l-1,2)-\boldsymbol{M}(l,2)$
NEGATIVE	NEGATIVE

Table 7.12: Values of θ_1 and g in case III.

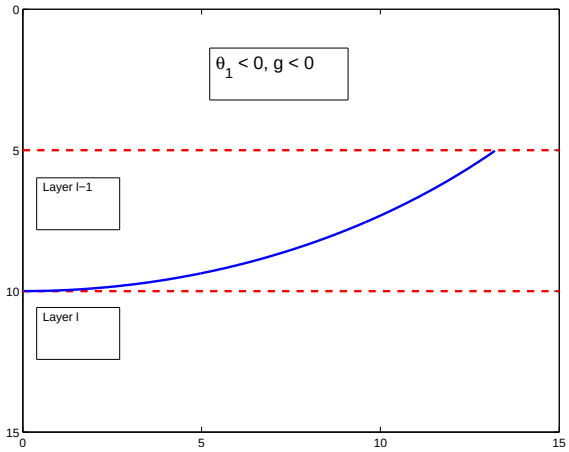

Figure 7.3: Ray behaviour in case III

The computations for case III are similar to case II. As in case II the algorithm only needs to determine whether the ray intersects a boundary, which in case III is

the surface or whether it continues to the next layer. If the ray intersects the surface values in Table 7.13 are computed. If the ray continues to the next layer values in Table 7.14 are computed.

$l = 2$	
g	$(\boldsymbol{M}(l-1,2) - \boldsymbol{M}(l,2))/(\boldsymbol{M}(l,1) - \boldsymbol{M}(l-1,1))$
r	$-(\boldsymbol{M}(l,2))/(g \cdot \cos\theta_1)$
θ_2	$\arccos(\boldsymbol{M}(l-1,2)/\boldsymbol{M}(l,2)) \cdot \cos(\theta_1)$
dx	$(\boldsymbol{M}(l-1,1) - \boldsymbol{M}(l,1)) \cdot \cot((\theta_1+\theta_2)/2)$
d	$-r \cdot (\theta_1+\theta_2)$
t	$t - 1/g \cdot \lvert \ln(\tan(\pi/4 - \theta_2/2)/\tan(\pi/4 - \theta_1/2))\rvert$
l	$l-1$
ϕ	$\phi + \pi$

Table 7.13: Rest of the variables for case III when next layer is surface.

else	
g	$(\boldsymbol{M}(l-1,2) - \boldsymbol{M}(l,2))/(\boldsymbol{M}(l,1) - \boldsymbol{M}(l-1,1))$
r	$-(\boldsymbol{M}(l,2))/(g \cdot \cos\theta_1)$
θ_2	$-\arccos(\boldsymbol{M}(l-1,2)/\boldsymbol{M}(l,2)) \cdot \cos(\theta_1)$
dx	$(\boldsymbol{M}(l-1,1) - \boldsymbol{M}(l,1)) \cdot \cot((\theta_1+\theta_2)/2)$
d	$-r \cdot (\theta_1+\theta_2)$
t	$t - 1/g \cdot \lvert \ln(\tan(\pi/4 - \theta_2/2)/\tan(\pi/4 - \theta_1/2))\rvert$
l	$l-1$
ϕ	ϕ

Table 7.14: Rest of the variables for case III when ray continues to the next layer.

Case IV

The ray is traveling towards the surface and the speed of sound increases. This is the same situation as in case II except for the direction of the ray. The signs for the ray angle and the sound speed gradient are given in Table 7.15.

Angle θ_1	Change in the speed of sound $\boldsymbol{M}(l-1,2) - \boldsymbol{M}(l,2)$
NEGATIVE	POSITIVE

Table 7.15: Values of θ_1 and g in case IV.

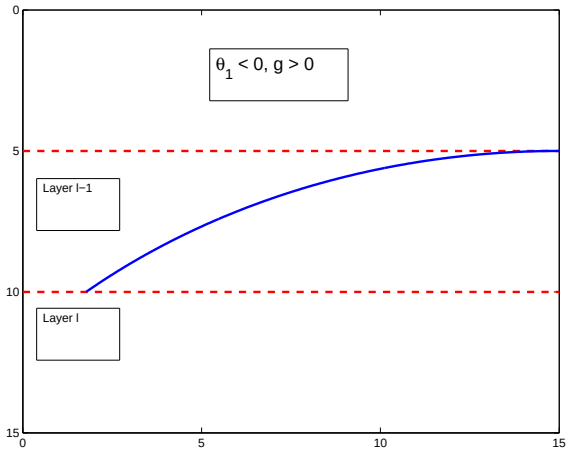

Figure 7.4: Ray behaviour in case IV.

The computations for case IV are similar to case I. First the program computes values for the two variables given in Table 7.16.

g	$(\boldsymbol{M}(l-1,2) - \boldsymbol{M}(l,2))/(\boldsymbol{M}(l,1) - \boldsymbol{M}(l-1,1))$
r	$(\boldsymbol{M}(l,2))/(g \cdot \cos\theta_1)$

Table 7.16: Expressions for g and r in case IV.

As in case I after computing the values in Table 7.15 the algorithm proceeds to examine which of the three possibilities given in Tables 7.17-7.19 evaluates. If the ray is bend back by the sound speed gradient the values in Table 7.17 are computed. If the ray intersects the surface the values in Table 7.18 are computed. If the ray continues to the next layer values in Table 7.19 are computed.

$\boldsymbol{M}(l-1,2)\cdot\cos\theta_1 > \boldsymbol{M}(l,2)$	
θ_2	$-\theta_1$
dx	$-(2\cdot\boldsymbol{M}(l,2)\cdot\sin\theta_1)/(g\cdot\cos\theta_1)$
t	$t+2\cdot 1/g\cdot\lvert\ln(\tan(\pi/4-\theta_1/2))\rvert$
d	$-r\cdot 2\cdot\theta_1$
ϕ	ϕ

Table 7.17: Rest of the variables for case IV when ray bends back.

$l=2$	
θ_2	$-\arccos(\boldsymbol{M}(l-1,2)/\boldsymbol{M}(l,2))\cdot\cos(\theta_1)$
dx	$(\boldsymbol{M}(l-1,1)-\boldsymbol{M}(l,1))\cdot\cot((\theta_1+\theta_2)/2)$
d	$-r\cdot(\theta_1+\theta_2)$
t	$t+1/g\cdot\lvert\ln(\tan(\pi/4-\theta_2/2)/\tan(\pi/4-\theta_1/2))\rvert$
l	$l-1$
ϕ	$\phi+\pi$

Table 7.18: Rest of the variables for case IV when next layer is surface.

else	
θ_2	$-\arccos(\boldsymbol{M}(l-1,2)/\boldsymbol{M}(l,2))\cdot\cos(\theta_1)$
dx	$(\boldsymbol{M}(l-1,1)-\boldsymbol{M}(l,1))\cdot\cot((\theta_1+\theta_2)/2)$
d	$-r\cdot(\theta_1+\theta_2)$
t	$t+1/g\cdot\lvert\ln(\tan(\pi/4-\theta_2/2)/\tan(\pi/4-\theta_1/2))\rvert$
l	$l-1$
ϕ	ϕ

Table 7.19: Rest of the variables for case IV when ray continues to the next layer.

Computing the New Coordinates

After each case I-IV new x, y coordinates are computed. The new x coordinate is computed as follows

$$x_{i+1} = x_i + dx,$$

and the new y coordinate becomes

$$y_{i+1} = \boldsymbol{M}(l, 1).$$

7.2 The Acoustics Toolbox

This section describes the use of the Acoustics Toolbox. Since only the normal mode program KRAKEN, the ray tracing program BELLHOP, and the acoustic field calculator program FIELD are used in this work, discussion of the rest of the models and functionality offered by the Acoustics Toolbox is omitted.

7.2.1 Structure

The structure of the Acoustic Toolbox as used in this work is best described by Figure 7.5. All models use ENVFIL as an input to describe the problem. ENVFIL has the same structure for all models with the exception of model specific attributes. KRAKEN produces the normal modes in a file named MODFIL. MODFIL and FLPFIL are used as inputs for FIELD which computes the transmission loss as function of range and depth in a file named SHDFIL. FLPFIL includes the necessary field parameters which for example determine how many of the available modes are used to compute the shade file SHDFIL. BELLHOP already outputs the necessary SHDFIL for analyzing the transmission loss.

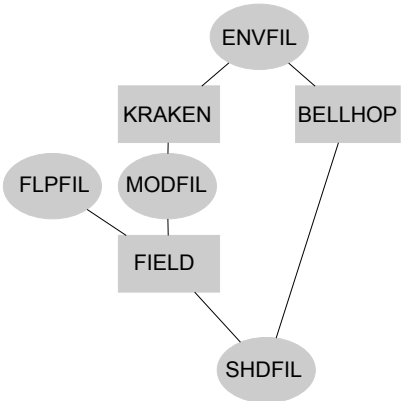

Figure 7.5: The structure of the Acoustics Toolbox. Circles represent input and output files, rectangles executables.

7.2.2 Environmental File

Listing 7.1 shows an example environmental file used by both KRAKEN and BELLHOP. Comments have been added to the file according to the Fortran 90 notation with exclamation marks.

Listing 7.1: Listing of an example environmental file

```
1  'SCENARIO_12_12'                          ! TITLE
2  250.000000                                ! FREQ (Hz)
3  1                                         ! NMEDIA
4  'NVM'                                     ! OPTIONS
5  0 0.000000 24.000000                      ! NMESH SIGMA (m) Z(NSSP)
6  0.000000 1477.000000 0 1.024000/          ! Z(m) CP CS(m/s) RHO(gm/cm3)
7  ! 22 LINES OMITTED
8  24.000000 1433.000000 /
9  'R' 0.0                                   ! BOTOPT SIGMA (m)
10 0.000000 1550.000000 /                    ! CLOW CHIGH (m/s)
11 1.500000                                  ! RMAX (km)
12 1                                         ! NSD
13 12.000000 /                               ! SD(1:NSD) (m)
14 1                                         ! NRD
15 12.000000 /                               ! RD(1:NDR) (m)
```

On line 1 the title of the environmental file is set. This title is optional and can be left blank by setting it to /,. Line 2 includes the frequency for which the environmental file is used. This frequency must be a single value and for a range of frequencies new environmental files must be created. Line 3 sets the number of media. For a single water body this value is set to 1. This setting does not affect the bottom or the surface media.

Line 4 includes the important model specific options. Each letter defines one option. In listing 7.1 the options are N for N2-linear interpolation used for the sound speed profile (SSP), V for a vacuum (pressure releasing) top boundary, and M for setting the attenuation unit to dB/m. Line 5 defines the number of vertical mesh points. When NMESH is set to 0 KRAKEN automatically defines the value of NMESH. SIGMA states the root mean squared (RMS) roughness of the surface. Z(NSSP) defines the depth of the waterbody.

On line 6 begins the SSP. On each line of the SSP Z(m) defines the depth at which the speed profile is defined. CP defines the P-wave speed or the speed of sound in water. CS defines the S-wave speed, but this setting can typically be ignored. RHO sets the water density. For the rest of the SSP only Z(m) and CP need to be defined. For readability 22 lines beginning from line 7 were omitted. These lines included the the rest of the speed profile for depths between zero and 24 metres.

Line 9 sets the bottom boundary condition BOTOPT and the bottom boundary roughness SIGMA. In this case BOTOPT was set to R for a perfectly rigid bottom.

Line 10 defines phase speed limits. CLOW sets the lower phase speed limit. By setting CLOW to 0 we let KRAKEN to automatically define the lowest phase speed. For CHIGH the larger the value, the longer the execution time since more modes are included. Line 11 defines the maximum range in kilometers.

Lines 12-15 define the source-receiver information. On line 12 NSD defines the number of source depths. Typically this value is set to 1. Line 13 defines the source depths. NRD on line 14 sets the number of receiver depths and the last line sets the

receiver depths.

7.2.3 Field Parameter File

Listing 7.2 shows an example field parameter file used by FIELD.

Listing 7.2: Listing of an example field parameter file

```
1  /,                      ! TITLE
2  'RA'                    ! OPT 'X/R', 'C/A'
3  9999                    ! M (number of modes)
4  1                       ! NPROF
5  0                       ! RPROF(1:NPROF) (km)
6  4094                    ! NR
7  0.100000 0.500000 /     ! R(1:NR)        (km)
8  1                       ! NSD
9  12.000000               ! SD(1:NSD)      (m)
10 1                       ! NRD            (m)
11 12.000000               ! RD(1:NRD)      (m)
12 1                       ! NRR            (m)
13 0.000000                ! RR(1:NRR)      (m)
```

Settings on lines 1 and 8-11 have already been discussed the previous section. On line 2 the options for source type and mode theory are selected. In Listing 7.2 the parameters used are R for point source and A for adiabatic mode theory. On line 3, M defines the number of modes to be used when computing the transmission loss. If this value exceeds the number of available modes in MODFIL then all the modes are used. Lines 4-5 define the profile ranges. NPROF sets the number of ranges where a new set of modes are used. In the typical case of range independent modes FIELD requires NPROF to be 1 and RPROF to be 0.

On line 6, NR defines the number of receiver ranges and on line 7, R(1:NR) defines the horizontal range in kilometres over which the transmission loss is computed. FIELD is limited to 4094 receiver ranges. In the example the maximum amount of receiver ranges are used. The transmission loss is then computed by FIELD in 4094 points between 100 and 500 metres.

7.2.4 Running the Programs

Both KRAKEN and BELLHOP are executed from the Windows command prompt. After the appropriate environmental and field files are created the transmission loss (SHDFIL) can be computed with KRAKEN as follows: kraken.exe < ENVFIL; field.exe < FLPFIL. For BELLHOP the execution is: bellhop.exe < ENVFIL. field.exe assumes that kraken.exe has been executed and that MODFIL exists.

8. RESULTS AND DISCUSSION

In this chapter the results on the transmission losses are presented. The numerical models of Chapter 7 were individually tested against a set of parameters which simulated a plausible source-receiver geometry with an equally plausible sound speed profile. The geometry includes both the source and the target depths, the time varying distance between the two, and a constant sea water depth. For the sound speed profile real measurements from three location across the Finnish coast were selected. These parameters are further discussed in the next section.

For KRAKEN and BELLHOP the transmission loss resulting from the source-receiver geometry can be recovered by analysing the output files of each program. For the Matlab versions, which includes the ideal and the refracted models, the transmission lossess are computed using the method described in Chapter 6.

8.1 Selection of Simulation Parameters

The simulated scenario consists of a submerged hydrophone and a submersible. The geometrical configuration of the hydrophone and the submersible follow the one presented in [19]. The hydrophone is set at a fixed location, both horizontally and vertically, while the submersible is fixed only vertically. As the submersible travels past the hydrophone the horizontal distance between the hydrophone and the submersible changes. This change in the horizontal distance also affects the properties of the acoustic multipath propagation. The source-hydrophone geometry is illustrated in Figure 8.1.

The parameters of the simulated scenario are presented in Table 8.1. The parameters were chosen to correspond to a situtation possible on the Finnish coast. The speed of the submersible was chosen to equal roughly one nautical mile per hour.

The length of the simulation was set to nine minutes or 540 seconds. The submersible makes its closest approach to the hydrophone at 175 seconds with a horizontal distance of 150 metres.

For the sound speed profiles real hydrographic profiles were used. The hydrographic profiles included the monthly temperature and salinity distribution of the water body at three locations on the Finnish coast and were obtained from [9]. The locations selected are Harmaja, Santio and Utö. From the hydrographic data sound speed profiles were computed using equation 3.3. The locations are shown on map

in Figure 8.2 and the sound speed profiles computed are shown in Figure 8.3 as a function of depth and month. The seawater depths of the locations are following: Harmaja 30m, Santio 40m and Utö 80m.

The seabed was modeled as a rigid surface with no transmission loss. The transmission loss due to geometrical spreading was modeled using cylindrical spreading. The absorption loss as a function of range or frequency was not taken into account.

Hydrophone depth	20 metres
Source depth	12 metres
Source speed	0.5 metres per second
Distance of closest approach	150 metres
Time of closest approach	175 seconds

Table 8.1: Simulation parameters.

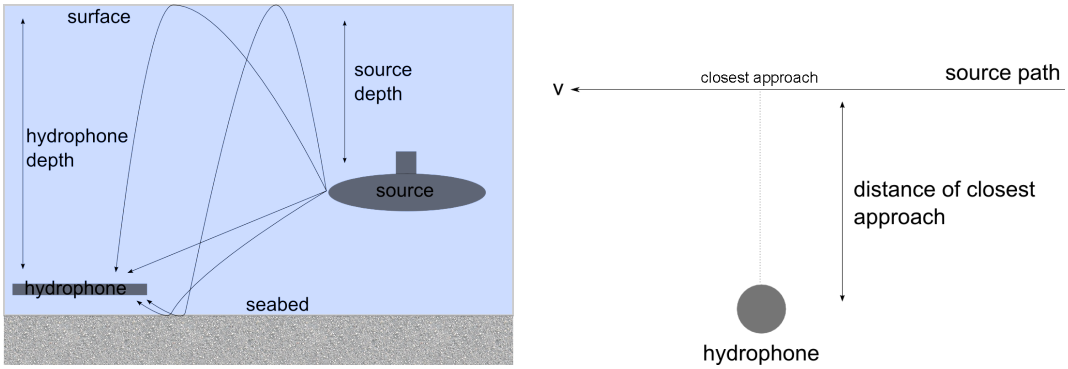

Figure 8.1: Geometry of the simulation. Cross-sectional view on the left, plane view on the right.

Figure 8.2: Map of the simulated locations. Harmaja 1, Santio 2 and Utö 3.

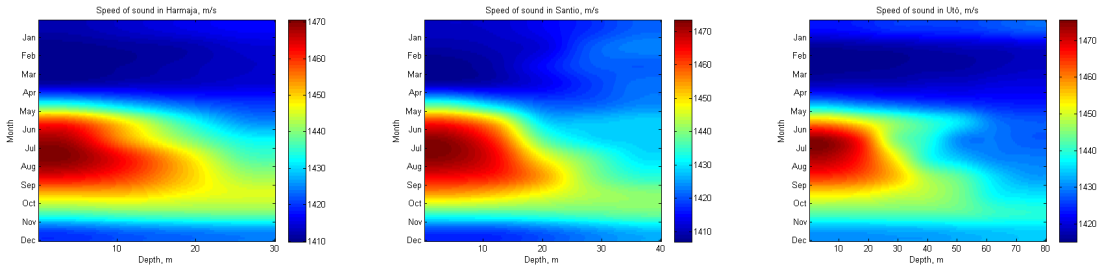

Figure 8.3: Sound speed profiles starting from left Harmaja, Santio and Utö.

8.2 Monthly Variation in the Interference Images

Figures 8.4-8.15 show the the computed interference images for each numerical model with simulation parameters from Table 8.1. The monthly variation in the transmission loss patterns is further illustrated in Figures 8.16-8.27 where a single time instant is plotted for both January and September. The time instant chosen is at 300 seconds in the full interference images.

The computation of the interference images was done using Algorithm 1 with the time delay, phase, and amplitude information gathered from rayTrace and the ideal model. For the ideal model this task was trivial. For the third party models provided by the Acoustics Toolbox, the interference images were compiled by plotting the transmission loss information. This information was accessed using Matlab functions to read the shade files produced by both KRAKEN and BELLHOP.

With rayTrace the computing of the interference image was done as follows. The ray tracer was set to compute a set of rays originating from the hydrophone. For each intersection between a ray and the source depth, the ray's time-of-flight, amplitude, and phase information was collected. Usually, each ray intersects the source depth multiple times at multiple different horizontal locations before reaching the termination line at some specified horizontal distance. At every new intersection, the ray usually represents a different route between the hydrophone and the target. Sometimes, the ray may bend around the target depth without reaching the surface or the bottom. In this case the ray will not represent a new route. In most of the cases the following example is valid: the first intersection with the target depth might be along a direct path, the second along a surface reflected path, the third along a surface-bottom reflected path and so on. This way a single ray can be made to produce information about multiple different routes between the source and the hydrophone. Using enough rays, a set of intersection points can be acquired for a number of horizontal distances and different routes. The rest can be interpolated using Matlab's own interpolation functions.

For each location the SSP was computed using the respected hydrographic data from the months of January and September. For Algorithm 1 all the available mul-

tipath routes were used to compute the interference image. The rays were computed with launch angles of $-70, \ldots, 70$ degrees. With the ideal model given in equation 5.3 delays were computed with $i = 1, 2, 3, \ldots, 15$. For BELLHOP and KRAKEN the SSP interpolation was set to N2-linear. The top boundary was modeled as a pressure releasing interface and for BELLHOP and KRAKEN the attenuation unit was set to dB/m. Other attenuation effects were disregarded. Example listings of the environmental files for BELLHOP and KRAKEN are given in Appendix A. Also an example field parameter file used by FIELD is given in Appendix A. For rayTrace and the ideal model the interference images range from $0 - 2500$ Hz. For BELLHOP and KRAKEN the interference images are computed between $50 - 2500$ Hz. This was due to the behaviour of KRAKEN which was unable to compute the normal modes at very low frequencies. In all Figures 8.4-8.15 the transmission loss is given in decibel scale.

For all models, excluding the ideal model which disregards refraction, the monthly change in the interference patterns is comparable. For the ideal model the change appears as a shift along the frequency axis while the rest of the models display more irregular changes.

The normal mode model used by KRAKEN is substantially different in approach compared to the rest, as can be seen in Figures 8.13-8.15 and 8.25-8.27. The other models are basically capable of finding an unlimited number of reflection paths while KRAKEN is restricted to the most prominent ones. The disparity between these models can be reduced by limiting the number of reflection paths in the other models. In Figure 8.28 the number of reflections for each path were limited to 3. The difference between rayTrace in Figure 8.28 and KRAKEN in Figure 8.27 is now significantly lower.

The rather large disparity between the results from the ideal and the refraction adjusted models indicate that for applications such as target parameter estimation the temperature profile should be taken into account. Then again, the monthly difference between the models themselves mean that the seasonal change in seawater temperature should also be taken into account.

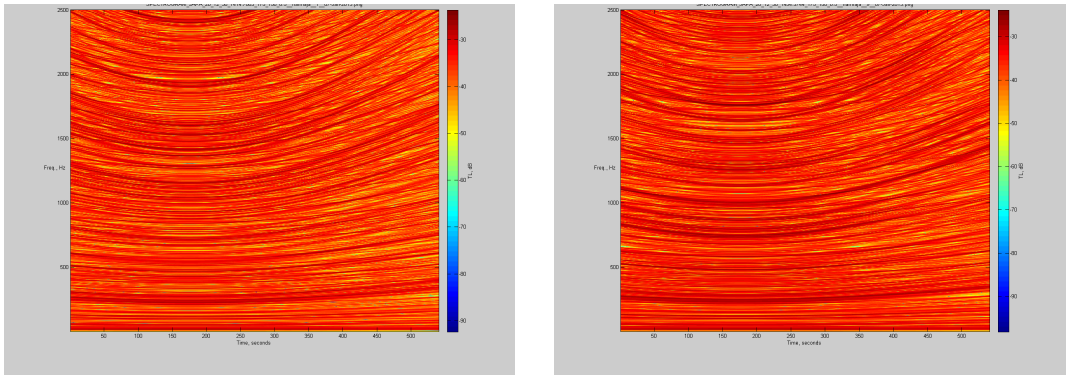

Figure 8.4: The interference image computed with rayTrace and Harmaja SSP using parameters from Table 8.1. Left in January, right in September. Water depth 30m.

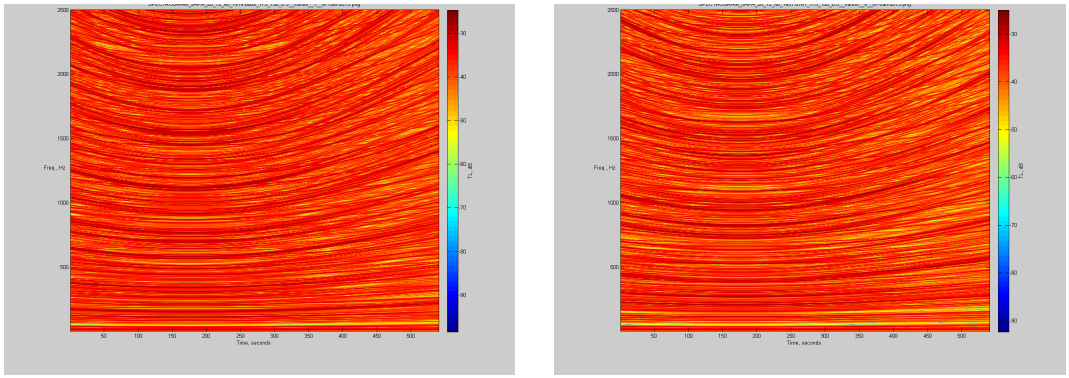

Figure 8.5: The interference image computed with rayTrace and Santio SSP using parameters from Table 8.1. Left in January, right in September. Water depth 40m.

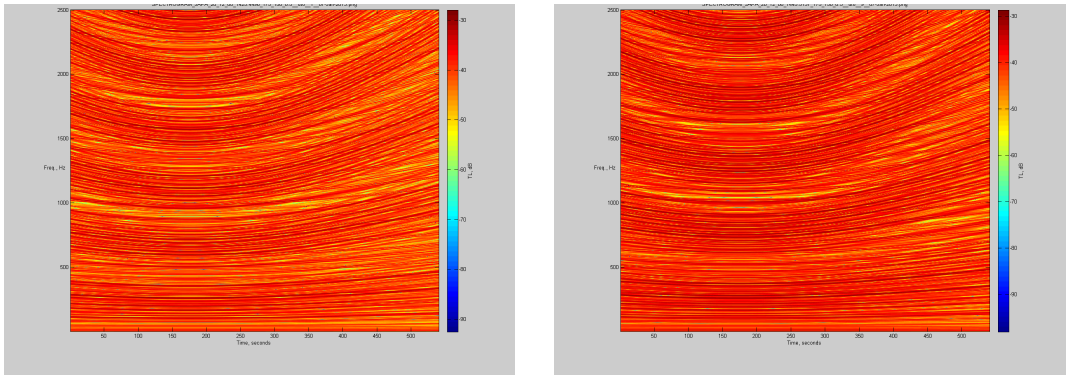

Figure 8.6: The interference image computed with rayTrace and Utö SSP using parameters from Table 8.1. Left in January, right in September. Water depth 80m.

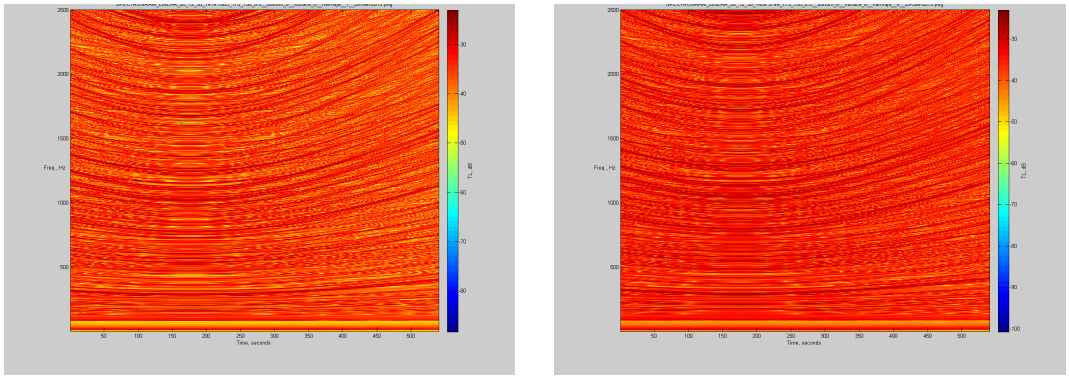

Figure 8.7: The interference image computed with the ideal model and Harmaja SSP using parameters from Table 8.1. Left in January, right in September. Water depth 30m.

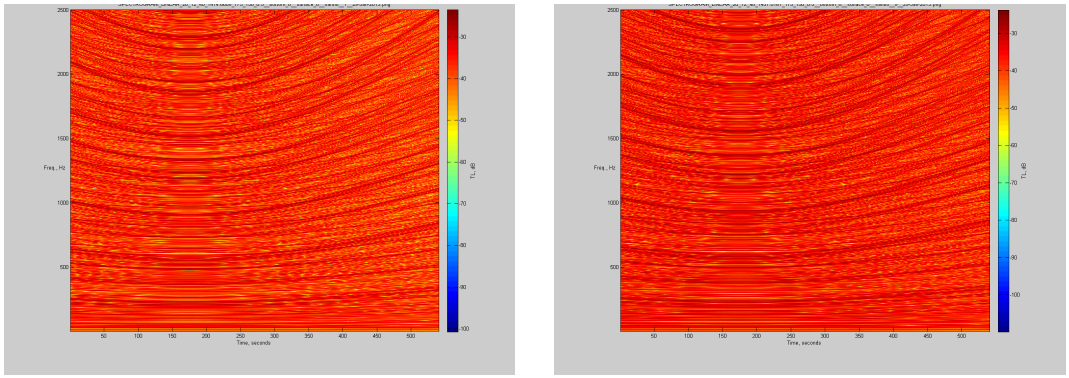

Figure 8.8: The interference image computed with the ideal model and Santio SSP using parameters from Table 8.1. Left in January, right in September. Water depth 40m.

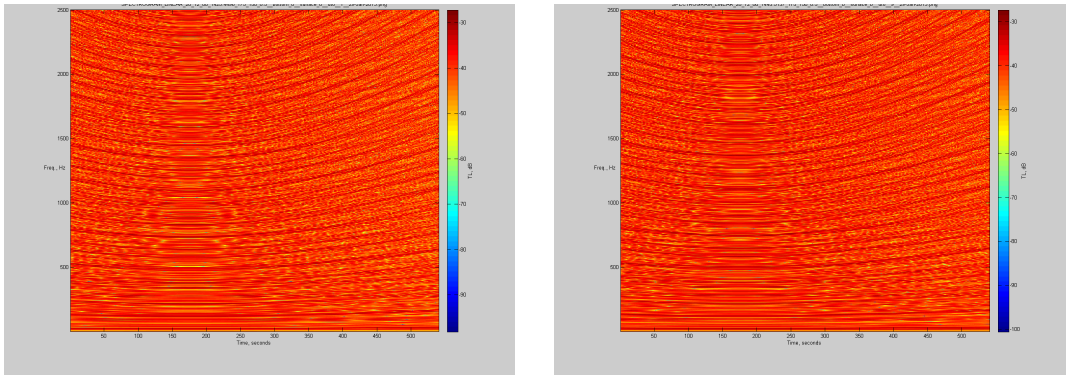

Figure 8.9: The interference image computed with the ideal model and Utö SSP using parameters from Table 8.1. Left in January, right in September. Water depth 80m.

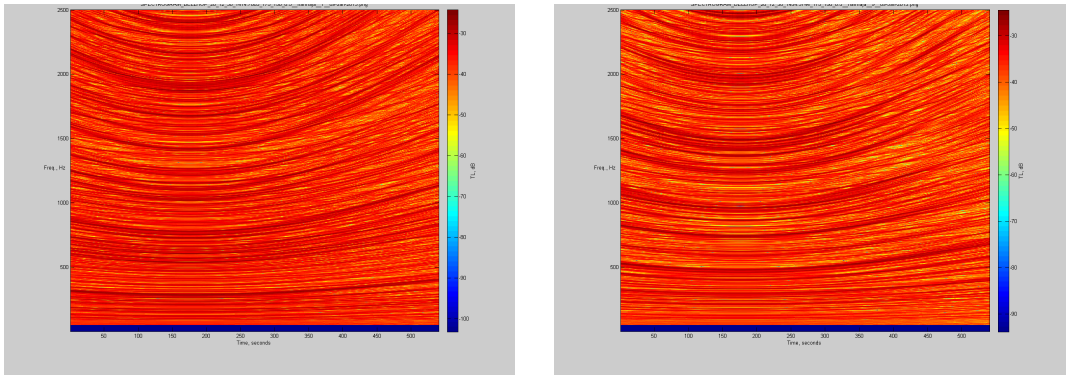

Figure 8.10: The interference image computed with BELLHOP and Harmaja SSP using parameters from Table 8.1. Left in January, right in September. Water depth 30m.

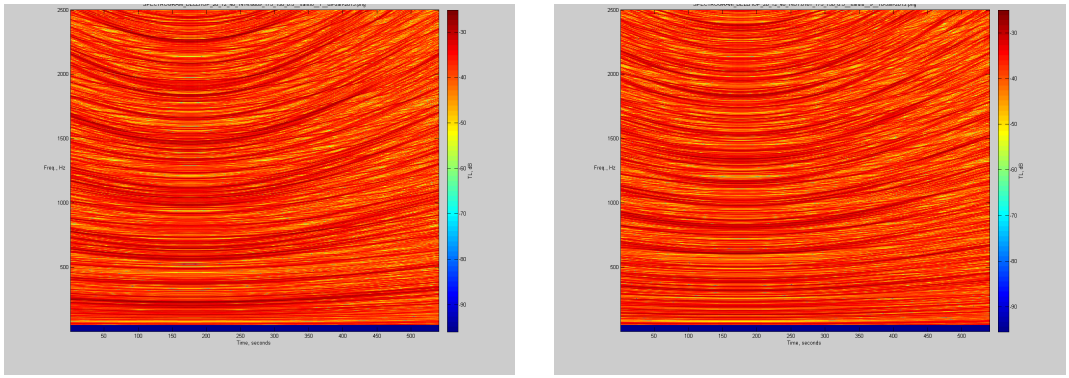

Figure 8.11: The interference image computed with BELLHOP and Santio SSP using parameters from Table 8.1. Left in January, right in September. Water depth 40m.

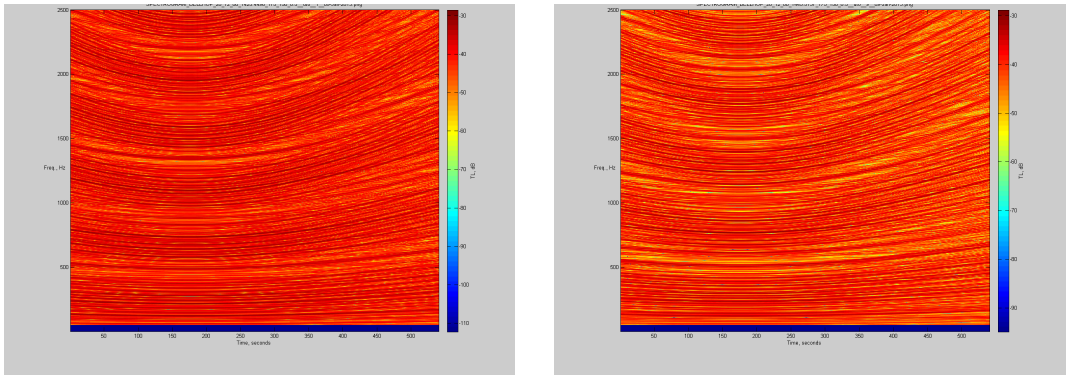

Figure 8.12: The interference image computed with BELLHOP and Utö SSP using parameters from Table 8.1. Left in January, right in September. Water depth 80m.

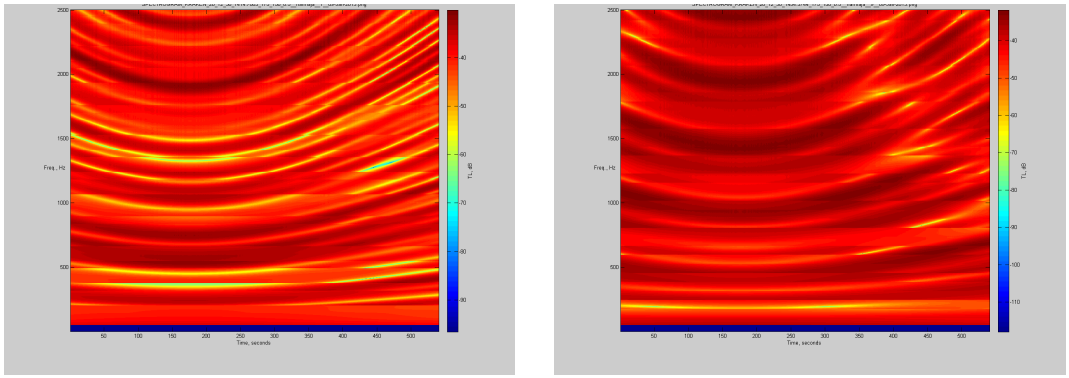

Figure 8.13: The interference image computed with the KRAKEN and Harmaja SSP using parameters from Table 8.1. Left in January, right in September. Water depth 30m.

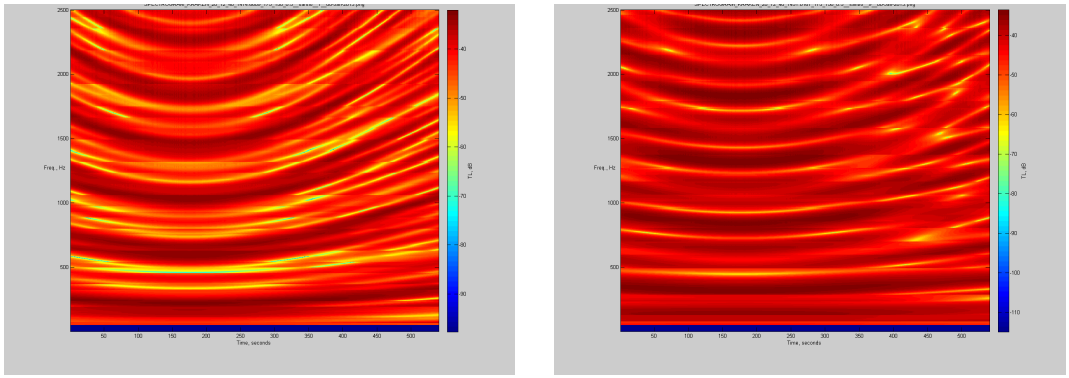

Figure 8.14: The interference image computed with KRAKEN and Santio SSP using parameters from Table 8.1. Left in January, right in September. Water depth 40m.

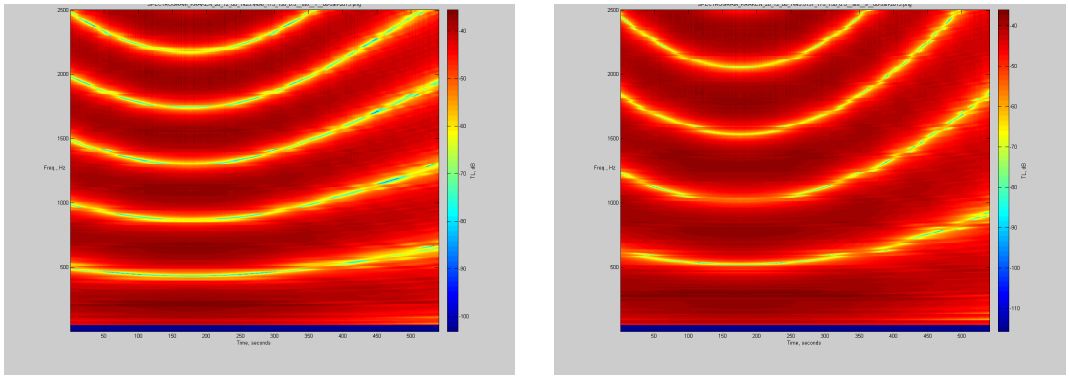

Figure 8.15: The interference image computed with KRAKEN and Utö SSP using parameters from Table 8.1. Left in January, right in September. Water depth 80m.

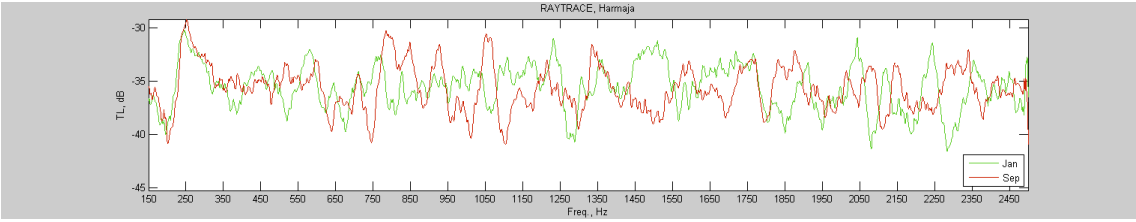

Figure 8.16: Monthly variation in the transmission loss computed with rayTrace between January and September in Harmaja using parameters from Table 8.1. Water depth 30m.

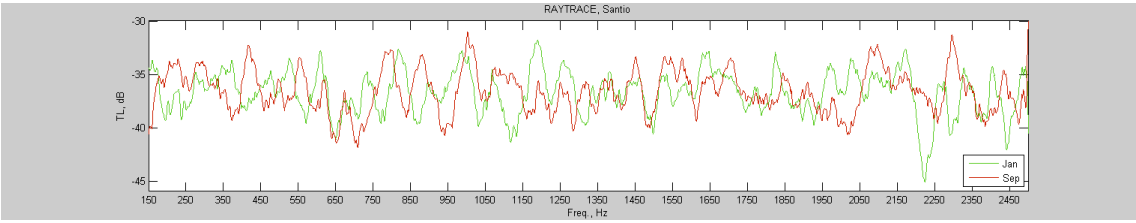

Figure 8.17: Monthly variation in the transmission loss computed with rayTrace between January and September in Santio using parameters from Table 8.1. Water depth 40m.

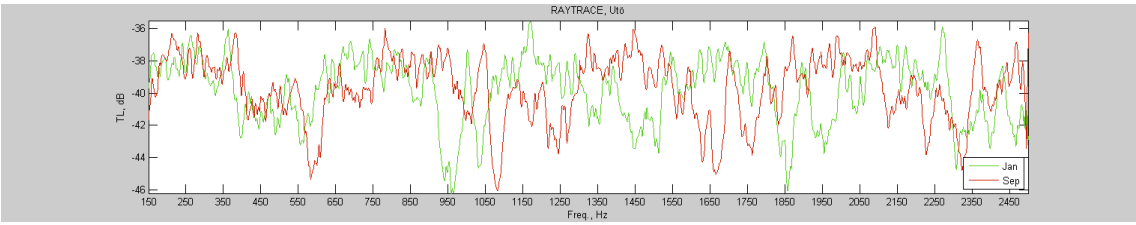

Figure 8.18: Monthly variation in the transmission loss computed with rayTrace between January and September in Utö using parameters from Table 8.1. Water depth 80m.

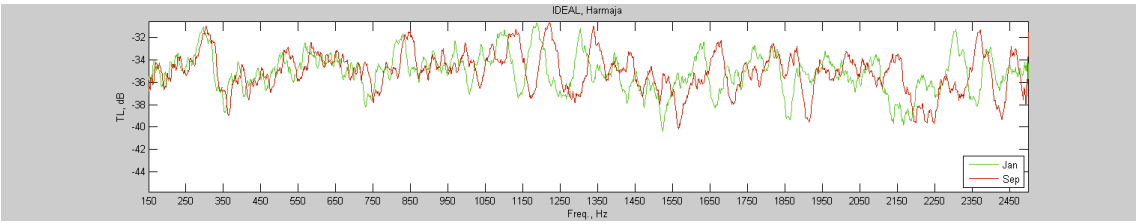

Figure 8.19: Monthly variation in the transmission loss computed with the ideal model between January and September in Harmaja using parameters from Table 8.1. Water depth 30m.

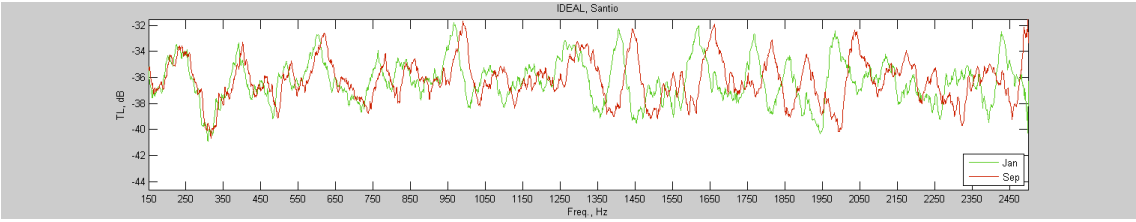

Figure 8.20: Monthly variation in the transmission loss computed with the ideal model between January and September in Santio using parameters from Table 8.1. Water depth 40m.

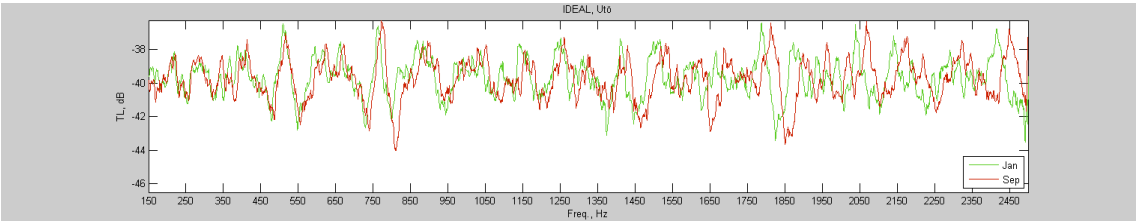

Figure 8.21: Monthly variation in the transmission loss computed with the ideal model between January and September in Utö using parameters from Table 8.1. Water depth 80m.

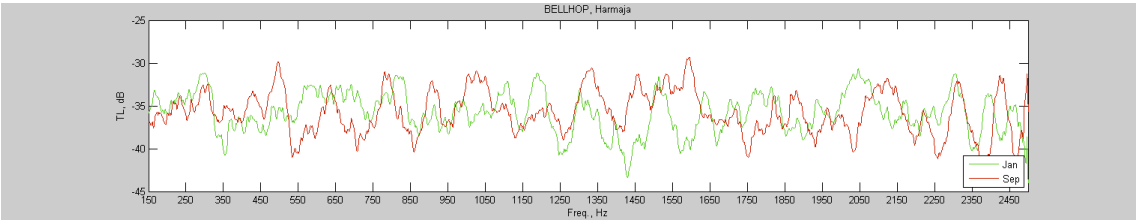

Figure 8.22: Monthly variation in the transmission loss computed with BELLHOP between January and September in Harmaja using parameters from Table 8.1. Water depth 30m.

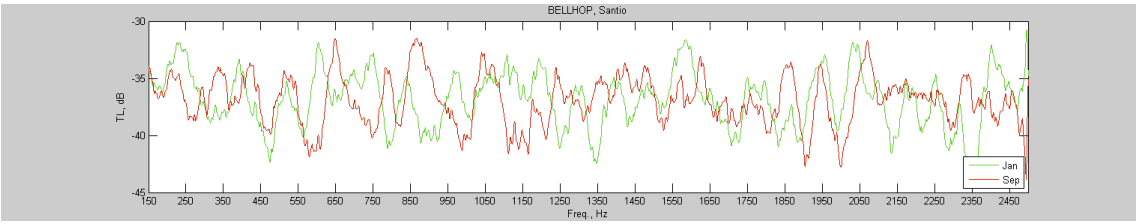

Figure 8.23: Monthly variation in the transmission loss computed with BELLHOP between January and September in Santio using parameters from Table 8.1. Water depth 40m.

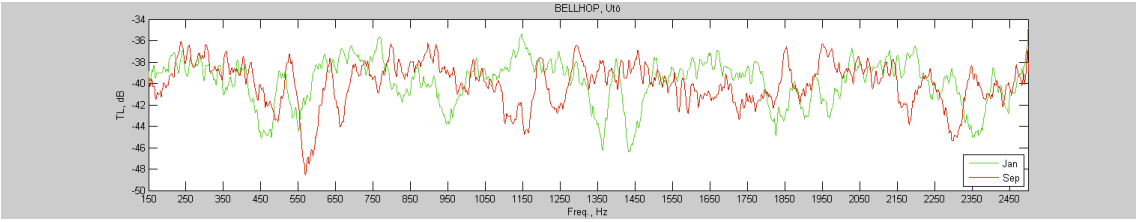

Figure 8.24: Monthly variation in the transmission loss computed with BELLHOP between January and September in Utö using parameters from Table 8.1. Water depth 80m.

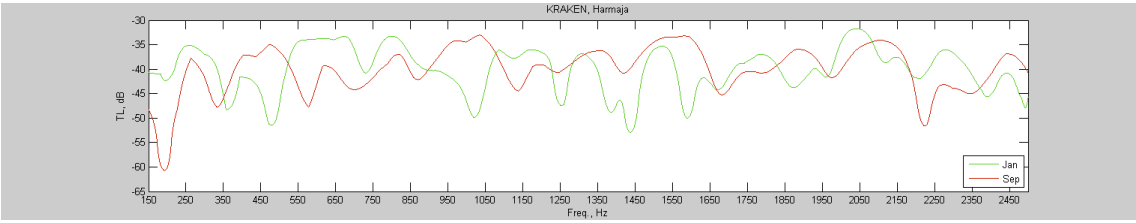

Figure 8.25: Monthly variation in the transmission loss computed with KRAKEN between January and September in Harmaja using parameters from Table 8.1. Water depth 30m.

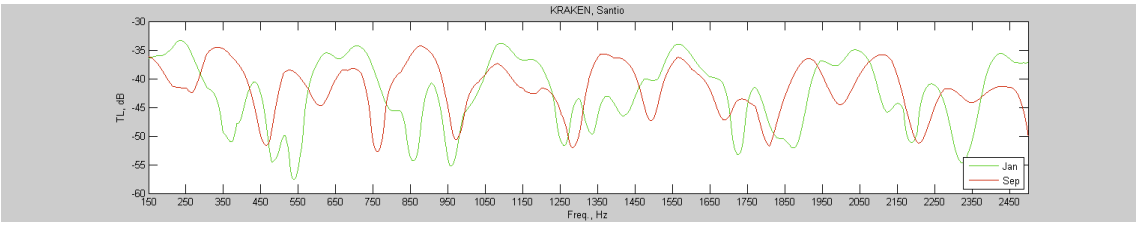

Figure 8.26: Monthly variation in the transmission loss computed with the normal KRAKEN between January and September in Santio using parameters from Table 8.1. Water depth 40m.

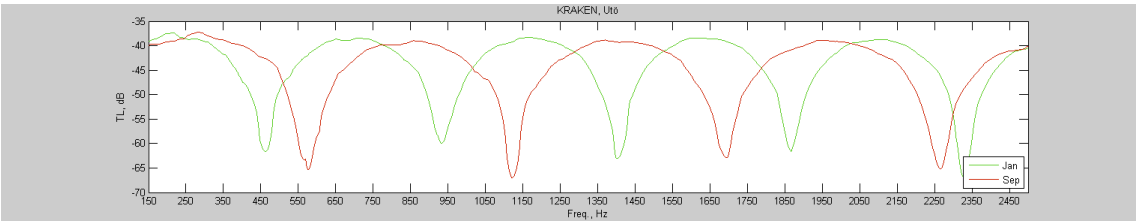

Figure 8.27: Monthly variation in the transmission loss computed with KRAKEN between January and September in Utö using parameters from Table 8.1. Water depth 80m.

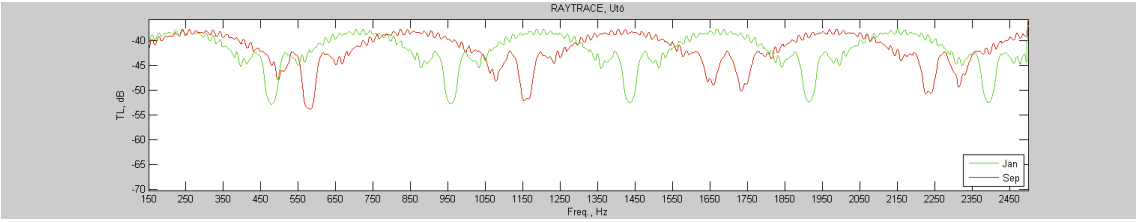

Figure 8.28: rayTrace with Utö SSP and the number of reflections per each path limited to 3 using parameters from Table 8.1. Water depth 80m.

8.3 Evaluating the Significance of Seabed Reflections

One notable previous study on shallow water interference images is [19] in which the effects of a single surface reflection were modeled. This single surface reflection is known as the Lloyd's mirror effect. One of the incentives for using Lloyd's mirror effect in classification of submerged vessels from surface ships is the assumption that the interference patterns detected can be confined to the context of surface reflections produced by underwater sound sources. If such interference patterns were also to be produced by the seabed the classification between submerged and surface ships becomes more complicated.

To assess this issue a surface ship was simulated using rayTrace and the parameters in Table 8.2. The location of the simulation was set to Santio and the month to July. The seabed reflection coefficient ranged from 0 to -9 dB and the surface reflection coefficient was set to 0 dB. To emulate a more realistic environment with ambient noise the interference images were hindered with noise. The signal-to-noise ratios (SNR) ranged from 42 to 60 dB.

With zero attenuation at the seabed boundary the interference pattern becomes visible with a SNR of 42 dB as can be seen from Figure 8.29. This figure also includes the results for the reflection coefficient at -1.5 and -3 dB. With the seabed reflection coefficient set to -1.5 dB some of the finer details disappear but the pattern still remains visible. The interference pattern is only barely visible when the seabed reflection coefficient reaches -3 dB. For higher SNR values the interference pattern remains clearly visible for reflection coefficients as low as -9 dB as can be seen from Figures 8.30-8.31.

These results indicate that theoretically a surface ship can produce an interference pattern comparable to that of the Lloyd's mirror effect of a submerged vessel. These results could be further improved with more advanced modeling of the seabed. Real seabeds rarely act as perfect reflectors nor do they have spatially constant reflection coefficients. Nevertheless, if the reflection does occur and the conditions are right then the interference pattern created by the surface ship could be mistaken for that of a submerged vessel.

Hydrophone depth	20 metres
Source depth	0 metres
Source speed	0.5 metres per second
Distance of closest approach	150 metres
Time of closest approach	175 seconds
Water depth	40 m
Bottom reflection coefficient	0 to −9 dB
Signal to noise ratio	42 to 60 dB

Table 8.2: Simulation parameters for the surface ship.

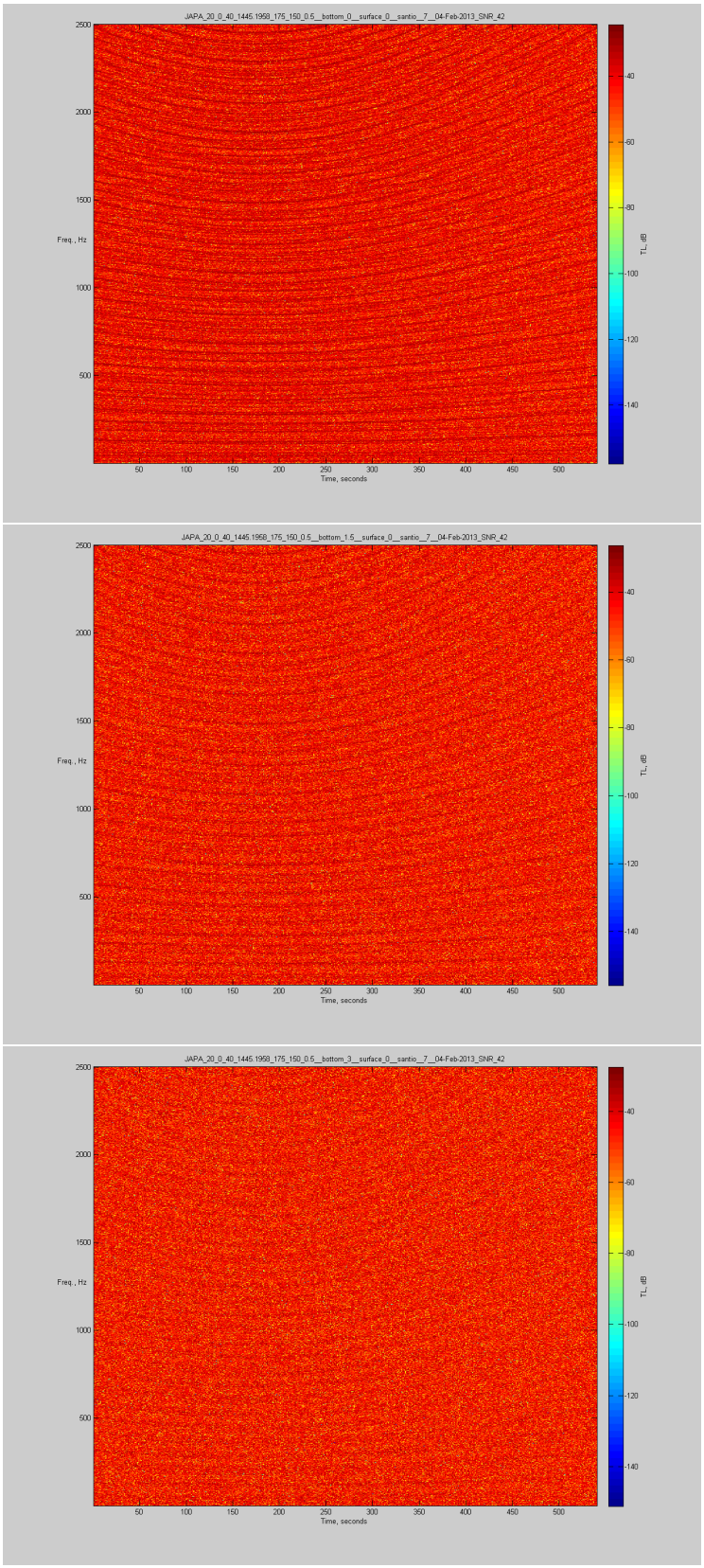

Figure 8.29: Interference image for the seabed reflection with a SNR of 42 dB. Bottom attenuation coefficient from the top 0, 1.5 and 3 dB.

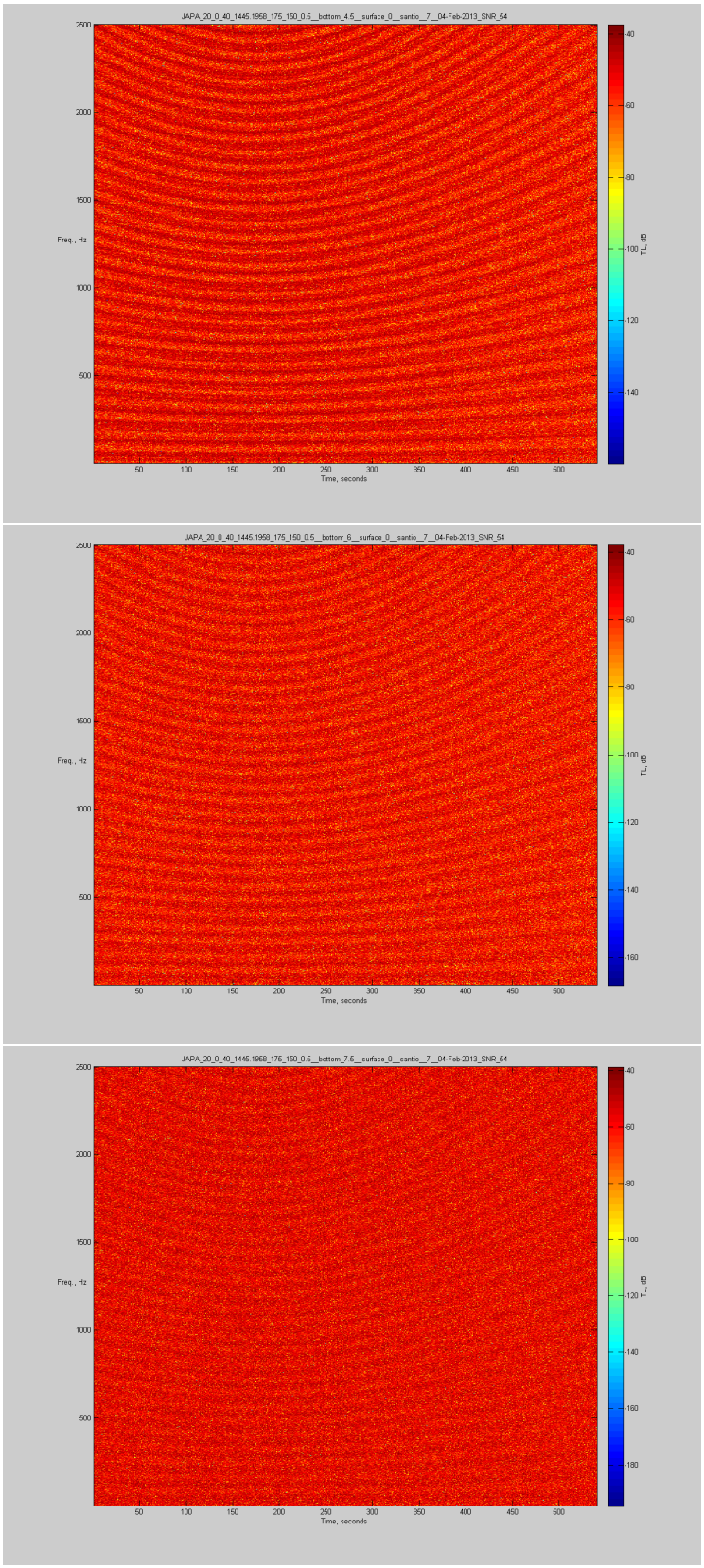

Figure 8.30: Interference image for the seabed reflection with a SNR of 54 dB. Bottom attenuation coefficient from the top 4.5, 6 and 7.5 dB.

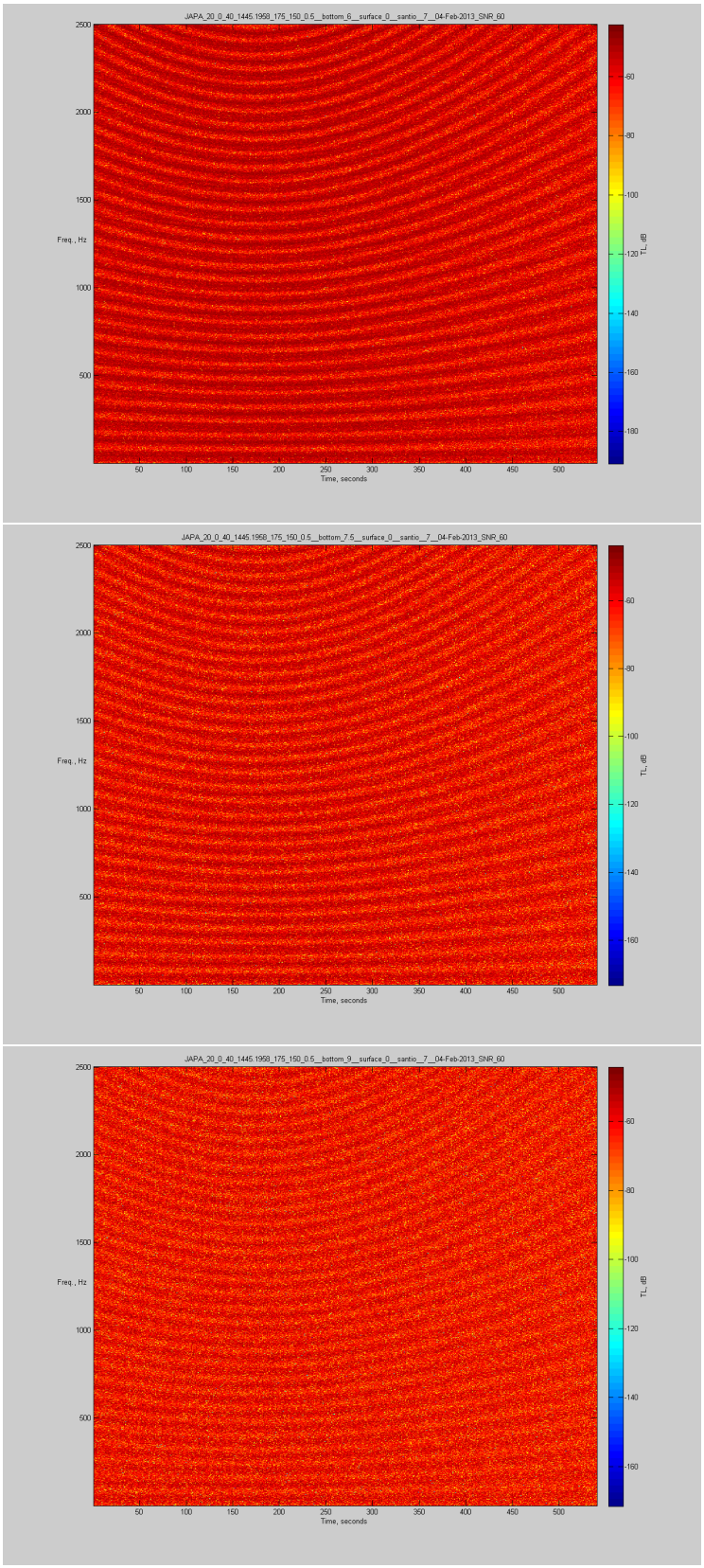

Figure 8.31: Interference image for the seabed reflection with a SNR of 60 dB. Bottom attenuation coefficient from the top 6, 7.5 and 9 dB.

9. CONCLUSIONS

In this work the multipath propagation of underwater sound was modeled using numerical models of ray and normal mode theories. The numerical models were used to estimate the transmission loss in shallow water. This transmission loss was studied in the form of interference patterns created by the constructive and destructive interference of the multipath environment. The interference patterns by the multipath delays were compiled into spectrograms using time-frequency analysis. A numerical ray model was developed in Matlab and used together with third party ray and normal mode models. The results were based upon a simulated target at three locations on the Finnish coast. The sound speed profiles for these locations were compiled from real hydrographic data acquired from the Finnish Institute of Marine Research.

The difference between the ideal and the refraction adjusted models was found to be significant. Also, the seasonal difference in the interference patterns was found to be equally significant. This indicates that rather accurate knowledge of the temperature profile of the water body is needed to be able to perform parameter estimation based on the interference patterns. Further, the seabed reflection was assessed in the context of the Lloyd's mirror effect. Lloyd's mirror effect can be used to discriminate between submerged vessels and surface ships by analysing the interference pattern created by a surface reflection known as the Lloyd's mirror effect. The results show that theoretically for a surface vessel the seabed reflection is enough to create interference patterns comparable to those of Lloyd's mirror. This on the other hand means that to distinguish between a surface and a submerged vessel one would have to be able to rule out the bottom reflection completely or at least somehow compensate for it. Also, the shape of the interference patterns could be further improved by incorporating the accurate formulas of Section 6.4.3 into the ray tracing algorithm.

BIBLIOGRAPHY

[1] C.T. Chen. *Digital Signal Processing: Spectral Computation and Filter Design*. The Oxford Series in Electrical and Computer Engineering Series. Oxford University Press, 2001.

[2] C.T. Chen and F. J. Millero. Speed of sound in seawater at high pressures. *The Journal of the Acoustical Society of America*, 62(5):1129–1135, 1977.

[3] J.W. Cooley and J.W. Tukey. An algorithm for the machine calculation of complex fourier series. *Mathematics of Computation*, 19:297–301, 1965.

[4] V.A. Del Grosso and Naval Research Laboratory (U.S.). *The velocity of sound in sea water at zero depth*. Washington, D.C. :U.S. Naval Research Laboratory,. http://www.biodiversitylibrary.org/bibliography/39225.

[5] R. Feistel, S. Weinreben, H. Wolf, S. Seitz, P. Spitzer, B. Adel, G. Nausch, B. Schneider, and D. G. Wright. Density and absolute salinity of the Baltic sea 2006-2009. *Ocean Science*, 6(1):3–24, 2010.

[6] N.P. Fofonoff and R.C. Millard. *Algorithms for Computation of Fundamental Properties of Seawater*. 1983.

[7] R.E. Gabler, J.F. Petersen, and L.M. Trapasso. *Essentials of Physical Geography*. Available Titles CengageNOW Series. Brooks/Cole, 2006.

[8] Research Analysis Group. *Physics of sound in the sea*. Number 1 in Physics of Sound in the Sea. Gordon and Breach, 1949.

[9] J. Haapala and P. Alenius. Temperature and salinity statistics for the northern Baltic sea 1961-1990. *Finnish Marine Research*, (262):51–121, 1994.

[10] F.B. Jensen, W.A. Kuperman, M.B. Porter, and H. Schmidt. *Computational Ocean Acoustics*. Modern Acoustics and Signal Processing. Springer, 2011.

[11] K.W. Lo, S.W. Perry, and B.G. Ferguson. Aircraft flight parameter estimation using acoustical Lloyd's mirror effect. *Aerospace and Electronic Systems, IEEE Transactions on*, 38(1):137–151, January 2002.

[12] X. Lurton. *An introduction to underwater acoustics : principles and applications*. Springer-Praxis books in geophysical sciences. Springer, New York, 2010.

[13] MathWorks. FFT, Fast Fourier Transform. [www], [referenced 14.12.2012], Available: `http://www.mathworks.se/help/matlab/ref/fft.html`.

[14] R.O. Nielsen. *Sonar signal processing.* Artech House acoustics library. Artech House, 1991.

[15] C.L Pekeris. *Theory of propagation of explosive sound in shallow water.* s.n., 1945.

[16] M.B. Porter. The kraken normal mode program (draft). [www], [referenced 6.11.2012], Available: `http://oalib.hlsresearch.com/Modes/AcousticsToolbox/manual_html/kraken.html`.

[17] R. Priemer. *Introductory Signal Processing.* Advanced Series in Electrical and Computer Engineering. World Scientific, 1991.

[18] R.J. Urick. *Principles of underwater sound.* McGraw-Hill, 1983.

[19] S.M. Viitanen. Passive detection of underwater targets using Lloyd's mirror effect. In *Proceedings of the 7th World Multiconference on Systemics, Cybernetics and Informatics SCI 2003*, pages 349–355, July 2003.

[20] W.D. Wilson. Speed of sound in sea water as a function of temperature, pressure, and salinity. *The Journal of the Acoustical Society of America*, 32(6):641–644, 1960.

[21] G.S.K. Wong and Shi ming Zhu. Speed of sound in seawater as a function of salinity, temperature, and pressure. *The Journal of the Acoustical Society of America*, 97(3):1732–1736, 1995.

[22] H.D. Young, R.A. Freedman, and A.L. Ford. *Sears and Zemansky's University Physics: With Modern Physics.* Pearson international edition. Pearson Addison-Wesley, 2008.

A. APPENDIX

Listing A.1: Environmental file for BELLHOP. Harmaja in September

```
'TEST_RUN'
500.000000
1
'NVM'
0 0.000000 30.000000
0.000000 1463.406684 0 1.024000/
1.000000 1463.259374 /
2.000000 1463.038973 /
3.000000 1462.749201 /
4.000000 1462.393779 /
5.000000 1461.976425 /
6.000000 1461.500860 /
7.000000 1460.970802 /
8.000000 1460.389973 /
9.000000 1459.762091 /
10.000000 1459.090876 /
11.000000 1458.380048 /
12.000000 1457.633327 /
13.000000 1456.854432 /
14.000000 1456.047082 /
15.000000 1455.214999 /
16.000000 1454.361901 /
17.000000 1453.491507 /
18.000000 1452.607539 /
19.000000 1451.713715 /
20.000000 1450.813755 /
21.000000 1449.911379 /
22.000000 1449.010306 /
23.000000 1448.114257 /
24.000000 1447.226951 /
25.000000 1446.352107 /
26.000000 1445.493445 /
27.000000 1444.654685 /
28.000000 1443.839547 /
29.000000 1443.051751 /
30.000000 1442.295015 /
'R' 0.0
1
12.000000
1
20.000000
4096
0.100000
0.500000/
'C'
64
-70.000000
```

```
70.000000/
1
31.000000
1.500000
```

Listing A.2: Environmental file for KRAKEN. Harmaja in September

```
'TEST_RUN'
500.000000
1
'NVM'
0 0.000000 30.000000
0.000000 1463.406684 0 1.024000/
1.000000 1463.259374 /
2.000000 1463.038973 /
3.000000 1462.749201 /
4.000000 1462.393779 /
5.000000 1461.976425 /
6.000000 1461.500860 /
7.000000 1460.970802 /
8.000000 1460.389973 /
9.000000 1459.762091 /
10.000000 1459.090876 /
11.000000 1458.380048 /
12.000000 1457.633327 /
13.000000 1456.854432 /
14.000000 1456.047082 /
15.000000 1455.214999 /
16.000000 1454.361901 /
17.000000 1453.491507 /
18.000000 1452.607539 /
19.000000 1451.713715 /
20.000000 1450.813755 /
21.000000 1449.911379 /
22.000000 1449.010306 /
23.000000 1448.114257 /
24.000000 1447.226951 /
25.000000 1446.352107 /
26.000000 1445.493445 /
27.000000 1444.654685 /
28.000000 1443.839547 /
29.000000 1443.051751 /
30.000000 1442.295015 /
'R' 0.0
0.000000 1550.000000 /
1.500000
1
12.000000 /
1
20.000000 /
```

Listing A.3: Field file for FIELD. Harmaja in September

```
/,
'RA'
9999
1
0
4094
```

```
0.100000  0.500000 /
1
12.000000
1
20.000000
1
0.000000
```